NASA TECHNICAL NOTE

NASA TN D-8080

NASA TN D-8080

A MATHEMATICAL MODEL OF AN ACTIVE CONTROL LANDING GEAR FOR LOAD CONTROL DURING IMPACT AND ROLL-OUT

John R. McGehee and Huey D. Carden

Langley Research Center
Hampton, Va. 23665

NATIONAL AERONAUTICS AND SPACE ADMINISTRATION • WASHINGTON, D. C. • FEBRUARY 1976

1. Report No.
NASA TN D-8080

2. Government Accession No.

3. Recipient's Catalog No.

4. Title and Subtitle
A MATHEMATICAL MODEL OF AN ACTIVE CONTROL LANDING GEAR FOR LOAD CONTROL DURING IMPACT AND ROLL-OUT

5. Report Date
February 1976

6. Performing Organization Code

7. Author(s)
John R. McGehee and Huey D. Carden

8. Performing Organization Report No.
L-10440

9. Performing Organization Name and Address
NASA Langley Research Center
Hampton, Va. 23665

10. Work Unit No.
743-01-12-03

11. Contract or Grant No.

12. Sponsoring Agency Name and Address
National Aeronautics and Space Administration
Washington, D.C. 20546

13. Type of Report and Period Covered
Technical Note

14. Sponsoring Agency Code

15. Supplementary Notes

16. Abstract

A mathematical model of an active control landing gear (ACOLAG) has been developed and programed for operation on a digital computer. The mathematical model includes theoretical subsonic aerodynamics; first-mode wing bending and torsional characteristics; oleo-pneumatic shock strut with fit and binding friction; closed-loop, series-hydraulic control; empirical tire force-deflection characteristics; antiskid braking; and sinusoidal or random runway roughness. The mathematical model was used to compute the loads and motions for a simulated vertical drop test and a simulated landing impact of a conventional (passive) main landing gear designed for a 2268-kg (5000-lbm) class airplane. Computations were also made for a simply modified version of the passive gear including a series-hydraulic active control system.

Comparison of computed results for the passive gear with experimental data shows that the active control landing gear analysis is valid for predicting the loads and motions of an airplane during a symmetrical landing. Computed results for the series-hydraulic active control in conjunction with the simply modified passive gear show that 20- to 30-percent reductions in wing force, relative to those occurring with the modified passive gear, can be obtained during the impact phase of the landing. These reductions in wing force could result in substantial increases in fatigue life of the structure.

17. Key Words (Suggested by Author(s))
Aircraft landing gear
Active controls
Landing loads

18. Distribution Statement
Unclassified – Unlimited

Subject Category 05

19. Security Classif. (of this report)
Unclassified

20. Security Classif. (of this page)
Unclassified

21. No. of Pages
70

22. Price*
$4.25

---

*For sale by the National Technical Information Service, Springfield, Virginia 22161

A MATHEMATICAL MODEL OF AN ACTIVE CONTROL LANDING GEAR FOR LOAD CONTROL DURING IMPACT AND ROLL-OUT

John R. McGehee and Huey D. Carden
Langley Research Center

SUMMARY

A mathematical model of an active control landing gear (ACOLAG) has been developed and programed for operation on a digital computer. The mathematical model includes theoretical subsonic aerodynamics; first-mode wing bending and torsional characteristics; oleo-pneumatic shock strut with fit and binding friction; closed-loop, series-hydraulic control; empirical tire force-deflection characteristics; antiskid braking; and sinusoidal or random runway roughness. The mathematical model was used to compute the loads and motions for a simulated vertical drop test and a simulated landing impact of a conventional (passive) main landing gear designed for a 2268-kg (5000-lbm) class airplane. Computations were also made for a simply modified version of the passive gear including a series-hydraulic active control system.

Comparison of computed results for the passive gear with experimental data shows that the active control landing gear analysis is valid for predicting the loads and motions of an airplane during a symmetrical landing. Computed results for the series-hydraulic active control in conjunction with the simply modified passive gear show that 20- to 30-percent reductions in wing force, relative to those occurring with the modified passive gear, can be obtained during the impact phase of the landing. These reductions in wing force could result in substantial increases in fatigue life of the structure.

INTRODUCTION

Dynamic loads in large aircraft resulting from landing impact and runway and taxiway unevenness are recognized as a significant factor in causing fatigue damage and dynamic stressing of the airframe structure. In addition, ground-induced vibrations result in crew and passenger discomfort and can contribute to reduction of the pilot's capability to control the aircraft. Such vibration problems have been encountered with some conventional transport aircraft and have required modification of the gear design to improve ride and handling qualities after the aircraft is in service.

These ground-induced dynamic loads and vibration problems will be magnified for supersonic-cruise aircraft because of the increased structural flexibility of the slenderbody, thin-wing designs and the higher takeoff and landing speeds. During design studies of supersonic transports conducted in the United States, investigations of the ground ride qualities of one particular design indicated extremely high vibration levels in the crew compartment during takeoff (ref. 1). The design philosophy for airplane oleo-pneumatic landing gears has been to obtain the lightest gear for the maximum designed sink rate. For supersonic-cruise transport aircraft, it may be necessary to concentrate on limiting the load applied to the structure by the gear to obtain satisfactory structural dynamic response characteristics and a satisfactory fatigue life. One potential method for improving ground operations of supersonic cruise aircraft is the application of active control technology to limit the loads applied to the airframe by the landing gears.

Analytical studies have been conducted to determine the feasibility of applying active controls to the landing gear during roll-out or taxiing over uneven runways or taxiways. The study reported in reference 2 indicated that a shock strut with a hydraulically controlled actuator in series with the passive elements of the strut (series-hydraulic control) possessed the most desirable dynamic properties and would be quite feasible to implement. Little published information is available for actively controlling loads applied to the airframe by the landing gear during the impact phase.

The purpose of this paper is to present and validate a mathematical model of an active control landing gear (ACOLAG) employing a series-hydraulic control for load control during impact and roll-out and to present results from the application of this control concept to a simply modified main landing gear of a 2268-kg (5000-lbm) class airplane. The model is evaluated for predicting airplane loads and motions encountered during vertical-drop and landing-impact simulations for a rigid airframe with a passive (conventional) oleo-pneumatic shock-strut landing gear. The model is also used to determine control parameters and airplane response for a series-hydraulic active control gear.

Edwin L. Fasanella, of LTV Aerospace Corporation, reviewed the equations of motion and assisted in debugging the antiskid braking and active control subroutines of the computer program.

SYMBOLS

The units used for the physical quantities defined in this paper are given first in the International System of Units and parenthetically in the U.S. Customary Units. Measurements and calculations were made in the U.S. Customary Units.

A_{co}	area of control orifice, m^2 (ft^2)
A_o	area of opening in shock-strut orifice plate, m^2 (ft^2)

A_p	cross-sectional area of metering pin, m^2 (ft^2)
A_1	shock-strut hydraulic area (piston area), m^2 (ft^2)
A_2	shock-strut pneumatic area (cylinder area), m^2 (ft^2)
AR	aspect ratio of wing, b^2/S_w
a	lift-curve slope at finite aspect ratio, $(dC_L/d\alpha)_{AR}$
a_∞	lift-curve slope for infinite AR, $dC_L/d\alpha$
b	wing span, m (ft)
$C_{D,f}$	aerodynamic friction-drag coefficient
$C_{D,i}$	aerodynamic induced-drag coefficient
$C_{D,p}$	aerodynamic profile-drag coefficient
$C_{d,co}$	discharge coefficient for control servo valve orifice
$C_{d,o}$	shock-strut orifice discharge coefficient
C_L	aerodynamic lift coefficient
C_X	numerical constant for each type of tire (this symbol is k_1 in ref. 3; type III, $C_X = 0.53$; type VII, $C_X = 0.60$)
C_Z	vertical-force coefficient for each type of tire (type I, $C_Z = 0.02$; types III and VII, $C_Z = 0.03$)
C_β	torsional damping coefficient of control sensor mass, N/rad-sec (lbf/rad-sec)

$C_{\beta,cr}$	critical torsional damping coefficient of control sensor mass, N/rad-sec (lbf/rad-sec)
D_f	fuselage aerodynamic drag force, N (lbf)
D_t	tail aerodynamic drag force, N (lbf)
D_w	wing aerodynamic drag force, N (lbf)
d	diameter of unloaded tire, m (ft)
d_{ce}	arm between airplane composite mass center and wing elastic axis in fuselage X_b-Z_b plane, m (ft)
d_{cf}	arm between airplane composite mass center and fuselage mass center in fuselage X_b-Z_b plane, m (ft)
$d_{c\ell}$	control-line diameter, m (ft)
d_{ct}	arm between airplane composite mass center and aerodynamic center of pressure of tail along X_b-axis, m (ft)
d_{cw}	arm between airplane composite mass center and wing mass center in fuselage X_b-Z_b plane, m (ft)
d_{cwG}	arm between airplane composite mass center and wing-gear interface in fuselage X_b-Z_b plane, m (ft)
d_{eh}	arm between wing elastic axis and hub in body coordinate system, m (ft)
d_{ew}	arm between wing elastic axis and wing mass center along X_b-axis, m (ft)
d_{wwG}	arm between wing mass center and wing-gear interface along X_b-axis, m (ft)
$dC_L/d\alpha$	lift-curve slope, rad^{-1}

d_1	arm between airplane composite mass center and wing-gear interface normal to Z_b-axis, m (ft)
d_2	distance between tire-runway interface and airplane composite mass center normal to X_g-axis, m (ft)
d_3	distance between airplane composite mass center and tail center of pressure parallel to fuselage longitudinal axis, m (ft)
d_4	distance between airplane composite mass center and fuselage mass center normal to fuselage longitudinal axis, m (ft)
d_5	distance between airplane composite mass center and wing center of pressure parallel to fuselage longitudinal axis, m (ft)
d_6	distance between airplane composite mass center and wing center of pressure normal to fuselage longitudinal axis, m (ft)
E	Young's modulus for wing structural material, Pa (lbf/ft^2)
e	base of natural logarithms
$F_{A,ss}$	total shock-strut axial force, N (lbf)
$F_{G,X}$	ground force at tire-runway interface acting along X_g-axis, N (lbf)
$F_{G,Z}$	ground force at tire-runway interface acting along Z_g-axis, N (lbf)
$F_{N,ss}$	force normal to shock strut, N (lbf)
F_n	nose-gear force along Z_g-axis, N (lbf)
$F_{ss,1}$	shock-strut binding friction force, N (lbf)
$F_{ss,2}$	sliding friction force between shock-strut piston and cylinder, N (lbf)

$F_{T,N}$	tire force normal to runway, N (lbf)
$F_{T,T}$	tire force tangential to runway, N (lbf)
F_{wB}	wing bending force due to cantilever deflection of wing, N (lbf)
G	shearing modulus of elasticity for wing structural material, Pa (lbf/ft^2)
g	gravitational acceleration, m/sec^2 (ft/sec^2)
h	height of wing box, m (ft)
I_a	mass moment of inertia of wheel and tire about axle, kg-m^2 (slug-ft^2)
I_e	mass moment of inertia of semispan of wing about elastic axis, kg-m^2 (slug-ft^2)
I_{sect}	area moment of inertia of wing chord section, m^4 (ft^4)
I_{YY}	pitching mass moment of inertia of one-half of airplane, with respect to plane of symmetry, about composite mass center, kg-m^2 (slug-ft^2)
K_{wB}	wing bending spring constant, N/m (lbf/ft)
$K_{w\tau}$	wing torsional spring constant, N-m/rad (lbf-ft/rad)
$K_{X,T}$	tire fore-and-aft spring constant, N/m (lbf/ft)
K_{β}	spring constant between braking control sensor mass and wheel, N/m (lbf/ft)
L_t	aerodynamic lift force of tail, N (lbf)
L_w	aerodynamic lift force of wing, N (lbf)
$l_{c\ell}$	length of active control hydraulic line, m (ft)

l_{ss}	shock-strut length, m (ft)
l_1	length between upper and lower shock-strut bearings for fully extended strut, m (ft)
l_2	length between lower shock-strut bearing and hub for fully extended strut, m (ft)
M_a	ground-induced torque on wheel about axle, N-m (lbf-ft)
M_{br}	brake torque about axle, N-m (lbf-ft)
M_{ef}	torque about wing elastic axis applied to fuselage, N-m (lbf-ft)
M_{ew}	torque about wing elastic axis applied to wing, N-m (lbf-ft)
M_n	nose-gear moment, N-m (lbf-ft)
m_c	composite mass, kg (slugs)
m_f	one-half of fuselage mass concentrated at fuselage center of gravity, kg (slugs)
m_h	mass assumed concentrated at hub (axle), kg (slugs)
m_w	semispan wing mass assumed concentrated at semispan wing c.g. on spanwise chord containing wing-gear interface, kg (slugs)
m_β	braking control sensor mass, kg (slugs)
N	number of cycles to failure
N_{Re}	Reynolds number of airflow
p	tire inflation pressure, Pa (lbf/ft^2)

p_{at}	atmospheric pressure, Pa (lbf/ft^2)
p_{ec}	effective active control pressure, Pa (lbf/ft^2)
p_H	hydraulic pressure, Pa (lbf/ft^2)
$p_{\ell c}$	control accumulator pressure, Pa (lbf/ft^2)
$p_{o,a}$	absolute tire inflation pressure at zero vertical load, Pa (lbf/ft^2)
p_r	rated inflation tire pressure, Pa (lbf/ft^2)
p_1	hydraulic pressure in shock-strut piston, Pa (lbf/ft^2)
p_2	pneumatic pressure in shock-strut cylinder, Pa (lbf/ft^2)
R_h	amplitude of runway roughness, m (ft)
r	deflected radius of tire, m (ft)
S_W	planform area of wing, m^2 (ft^2)
s	shock-strut stroke, m (ft)
t	elapsed time after touchdown, sec
V_{ac}	volume of hydraulic fluid transferred by active control, m^3 (ft^3)
V_2	volume enclosed by shock-strut cylinder, m^3 (ft^3)
v_{eff}	effective velocity of hydraulic fluid through control, m/sec (ft/sec)
v_{temp}	intermediate value of velocity of hydraulic fluid through control for computing pressure loss, m/sec (ft/sec)

w	maximum width of undeflected tire, m (ft)
x_b,x_g	displacement along X_b- or X_g-axis, m (ft)
x_{cp}	fore-and-aft shift of tire footprint center of pressure, m (ft)
y	absolute value of spanwise distance from fuselage center line to chord containing wing-gear interface, m (ft)
z_b,z_g	displacement along Z_b- or Z_g-axis, m (ft)
z_{Be}	bending deflection of wing elastic axis at spanwise chord of wing mass center relative to wing elastic axis at fuselage center line along Z_b-axis, m (ft)
$z_{er,b}$	relative displacement between wing elastic axis at spanwise chord containing wing mass center and wing elastic axis in fuselage X_b-Z_b plane along Z_b-axis, m (ft)
$z_{ew,b}$	displacement of wing elastic axis at spanwise chord containing wing mass center along Z_b-axis, m (ft)
$z_{G,g}$	ground elevation measured along Z_g-axis, m (ft)
z_ℓ	initial height along Z_g-axis between shock-strut fluid level and control-reservoir fluid level, m (ft)
α	total angular displacement of wing chord at spanwise location of wing mass center relative to wing chord at fuselage center line, $\alpha_i + \alpha_e$, rad
α_e	wing elastic rotation, rad
α_i	angle of incidence of wing, rad
β	angular displacement of brake sensor mass, rad
γ	ratio of specific heat of gas at constant pressure to that at constant volume
γ_H	specific weight of hydraulic fluid, N/m^3 (lbf/ft^3)

Δ	difference or change of value
δ	combined vertical tire deflection, m (ft)
δ_o	vertical tire deflection for pure vertical loading, m (ft)
δ_v	vertical sinking of tire due to fore-and-aft tire deflection, m (ft)
ζ	slip ratio between wheel and surface
η	slope of runway surface, rad
θ	angle of pitch of airplane, rad or deg
κ	tire pressure-rise parameter
λ_{ce}	angle, in X_b-Z_b plane, between wing chord and line connecting wing elastic axis to airplane composite mass center, rad
λ_{cf}	angle, in X_b-Z_b plane, between fuselage longitudinal axis and line connecting fuselage mass center to airplane composite mass center, rad
λ_{cw}	angle, in X_b-Z_b plane, between line connecting wing mass center to airplane composite mass center and line through composite mass center parallel to fuselage longitudinal axis, rad
λ_{cwG}	angle, in X_b-Z_b plane, between line connecting wing-gear interface to airplane composite mass center and line through composite mass center parallel to fuselage longitudinal axis, rad
λ_{eh}	angle, in X_b-Z_b plane, between Z_b-axis and line connecting wing elastic axis to hub, rad
μ	friction coefficient between tire footprint and runway surface, or tire-runway friction coefficient (positive along negative X_g-axis)
μ_H	dynamic viscosity of hydraulic fluid, N-sec/m^2 (lbf-sec/ft^2)
$\mu_{ss,l}$	friction coefficient between shock-strut lower bearing and piston

$\mu_{ss,u}$	friction coefficient between shock-strut upper bearing and cylinder
ρ_a	mass density of air, kg/m^3 (slugs/ft^3)
ρ_H	mass density of hydraulic fluid, kg/m^3 (slugs/ft^3)
σ	stress level, Pa (lbf/ft^2)
ϕ	angular displacement of wheel about axle, rad
ω_G	frequency of variation of sinusoidal runway elevation, rad/sec
$\omega_{n,\beta}$	natural frequency of brake control sensor mass, rad/sec

Subscripts:

b	body-axis system
c	airplane composite mass center
ce,b	between airplane composite mass center and wing elastic axis in body-axis system
e	wing elastic axis
f	fuselage mass center
g	gravity-axis system
h	hub mass center
i	initial value
max	maximum value
t-Δt	value at previous time step

w	wing mass center
wG	wing-gear interface
x	linear dimension along X_b-axis
z	linear dimension along Z_b-axis

Dots over symbols indicate differentiation with respect to time.

MATHEMATICAL MODEL

Variables considered significant in analyzing actively controlled landing gear systems are shown in figure 1. Of these variables the following are included in this study: impact loads; runway-induced loads; braking loads; aerodynamic loads; flexible-airframe characteristics; and load isolation. Some examples of previously proposed landing gear active control concepts for load isolation are shown in figure 2. The series-pneumatic and the series-hydraulic controls have the actuator in series with the stiffness and damping elements of the shock strut. The parallel-hydraulic control has the actuator in parallel with the stiffness and damping elements of the shock strut. In all these systems, control is implemented by metering the working fluid (oil or air) to the actuator. For the present analysis the series-hydraulic control was selected on the basis of results of the feasibility study presented in reference 2.

Three rigid-body degrees of freedom are included in the model: vertical translation, fore-and-aft translation, and pitching about the airplane mass center. Since the model was devised to study active control concepts of a single main gear with pitch rotation included, lateral symmetry was assumed and a simplified representation (linear spring with no rebound) of a nose gear was included to absorb the rotational energy. Definitions of axes and forces for the rigid-airframe option and for the rigid-fuselage—elastic-wing option are presented in figures 3 and 4, respectively. The model accounts for the following variables: sinusoidal or random runway unevenness; empirical tire force-deflection characteristics and antiskid braking; oleo-pneumatic strut with fit and binding friction; closed-loop, series-hydraulic control; first-mode wing bending and torsional structural-elastic characteristics; and theoretical subsonic aerodynamics without ground effect. These variables will be discussed in order in the following sections.

Runway Model

Two general methods of analysis for runway unevenness have been considered in the study reported in reference 4: deterministic and statistical (power spectral). It was stated in reference 4 that the deterministic approach should be used for dynamic analysis when the response characteristics of the airplane are nonlinear. Consequently, runway models included in the present analysis are a sinusoidal variation of runway elevation as a function of distance traversed along the runway or a random variation of runway elevation as a function of runway distance. For the sinusoidal variation, the runway elevation is defined in terms of the frequency and the amplitude of undulation as follows:

$$z_{G,g}\big|_t = R_h \sin (\pi + \omega_G t)$$

The slope of the runway surface at any instant in time is:

$$\eta\big|_t = \tan^{-1}\left[\frac{-\left(z_{G,g}\big|_t - z_{G,g}\big|_{t-\Delta t}\right)}{\dot{x}_{h,g}\big|_t \,\Delta t}\right]$$

The random variation of runway elevation is defined as piecewise linear slopes in terms of runway distance traversed as follows:

$$z_{G,g}\big|_t = f\left(\eta\big|_t, x_{G,g}\big|_t\right)$$

For the random variation a table of runway elevation as a function of distance traversed is required as input.

Tire and Brake Models

The tire and brake models employed in this analysis are shown in sketch (a):

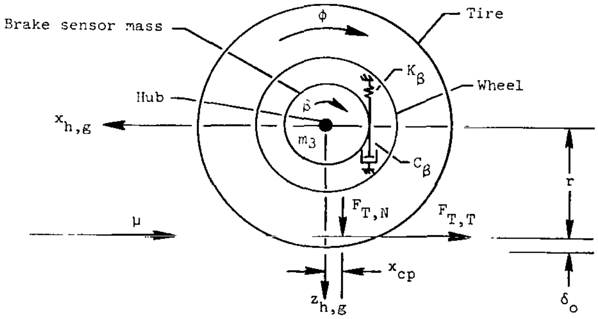

Sketch (a)

Empirical tire force-deflection equations.- The mechanical properties of the tire are defined from semiempirical equations given in reference 3. Equation (125) of reference 3 is used to define the normal tire force $F_{T,N}$ during a landing impact as a function of tire deflection and physical properties of the undeformed tire. This equation is (in the present notation)

$$F_{T,N} = 2.4\left[\frac{\delta}{w} - C_Z\left(1 - e^{\frac{-0.6\frac{\delta}{w}}{C_Z}}\right)\right]\left[p + 0.08p_r + \gamma\kappa p_{o,a}\left(\frac{\delta}{w}\right)^2\left(w\sqrt{wd}\right)\right]$$

where

$$\delta = \delta_o - \delta_v$$

$$\delta_v = 0.01\frac{F_{T,T}}{K_{X,T}}$$

$$K_{X,T} = C_X d(p + 4p_r)\left(\frac{\delta_o}{d}\right)^{1/3}$$

The tangential tire force $F_{T,T}$ during free rolling of the wheel is defined as that force required to decelerate the wheel such that the tire tangential velocity is equal to the hub velocity. The tangential tire force during skidding (slip ratios ζ greater than zero) is defined as the tire-runway friction coefficient μ multiplied by the normal tire force.

Tire-runway friction coefficient.- The tire-runway friction coefficients are modeled as a function of wheel-runway slip ratio ζ (called S_W in ref. 5) on the basis of experimental data presented in references 5 and 6. (See sketch (b).) The dashed line represents the model of the tire-runway friction coefficient at touchdown and during wheel spin-up. In the present analysis, the friction coefficient at touchdown is assumed to be 0.336 on the basis of data in reference 6. During wheel spin-up the tire-runway friction coefficient is held constant until the wheel slip ratio decreases to a value of 0.06 (sketch (b)), which is the intersection of the braking and spin-up curves. The friction coefficient is then reduced along the braking-model curve to the value of zero friction for free rolling. Antiskid braking is initiated at the time of nose-gear touchdown, and the friction coefficient follows the braking curve to a slip ratio of approximately 0.25. The antiskid braking system then operates with a sensor mass acceleration corresponding to the slip ratio (approximately 0.25) for maximum tire-runway friction coefficient.

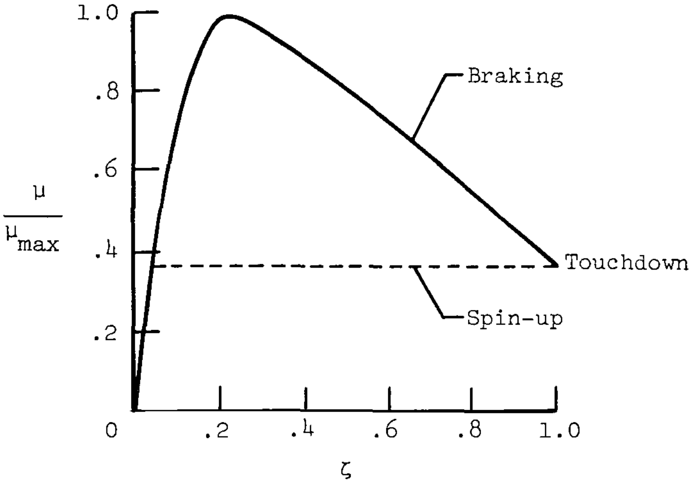

Sketch (b)

Braking model.- The antiskid braking system model presented in reference 5 was simplified in this paper by omitting the tire elasticity at the tire-wheel interface. The brakes are controlled by the angular acceleration of the control sensor mass, which is attached to the wheel through a spring-damper arrangement (sketch (a)). Brake application and release are controlled by preselected values of control-sensor-mass accelerations. The brake torque applied by the system is assumed to be torque limited; onset and offset torque rates may be independently changed, but vary linearly with time.

Oleo-Pneumatic Shock-Strut Model

A sketch of a typical oleo-pneumatic shock strut and a detailed description of the mechanics of the landing gear are presented in reference 7. During a landing impact the strut piston forces hydraulic fluid to flow through an orifice at a high velocity and creates a pressure drop across the orifice which resists the motion of the piston. (See fig. 2.) In addition to the hydraulic resistance to strut closure, the fluid flow into the strut cylinder increases the pneumatic (nitrogen) pressure, which also opposes strut closure. Internal bearing friction forces must also be considered along with the pressure forces. The total axial force developed by a passive (conventional) shock strut, with a metering pin, may be expressed as follows:

$$F_{A,ss} = (p_1 - p_2)(A_1 - A_p) + p_2A_2 + \frac{\dot{s}}{|\dot{s}|}(F_{ss,1} + F_{ss,2})|\tanh(2\dot{s})|$$

where

$$F_{ss,1} = \left(\mu_{ss,u} \frac{l_2 - s}{l_1 + s} + \mu_{ss,l} \frac{l_2 - s}{l_1 + s} + 1\right) F_{N,ss}$$

This is a modified form of the equation presented in reference 7. Since the shock strut connects the airframe and the hub, the axial force imposes acceleration to the airframe while reacting to hub motion.

Series-Hydraulic Active Control Gear Model

The purpose of the series-hydraulic active control gear is to limit the force applied to the airframe at the wing-gear interface by regulating the damping force in the oleo-pneumatic strut. The model of the series-hydraulic active control gear is shown schematically in sketch (c). The control consists of a servo valve, a high-pressure reservoir, a hydraulic pump, a low-pressure accumulator, an electronic control circuit, accelerometers, pressure transducers, and a linear potentiometer.

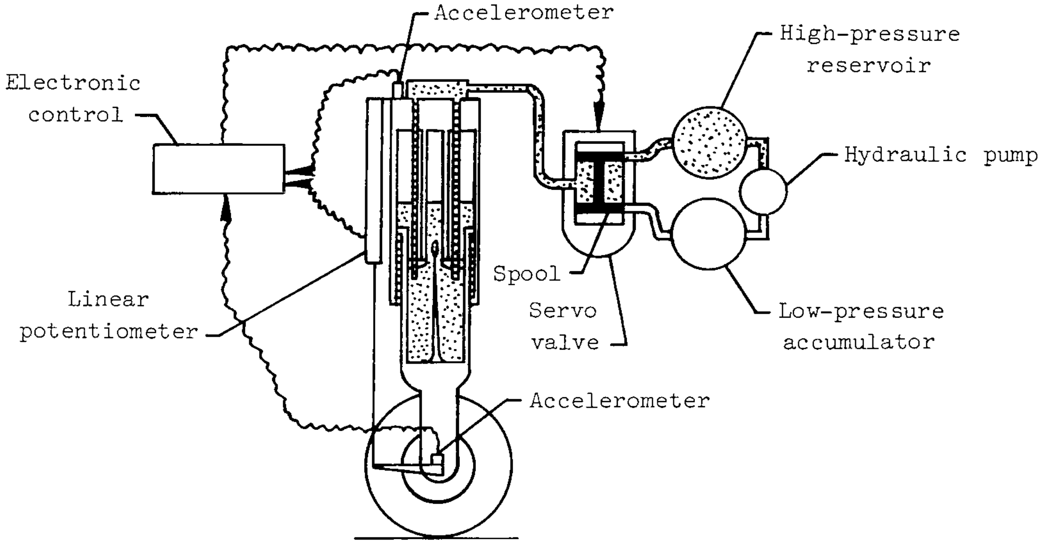

Sketch (c)

The following example illustrates the operation of the series-hydraulic active control gear during a landing impact and roll-out. The mass at the wing-gear interface is assumed to remain constant during landing; thus, the acceleration of the wing-gear interface reflects the force applied at this position. For a specific airplane design and the measured sink rate, the limit force, defined from the limit acceleration, is determined as the product of the mass and the square of the sink rate divided by the available shock-strut stroke. A signal corresponding to the limit acceleration is input to the electronic control circuit. The electronic control circuit (sketch (c)) continuously monitors the acceleration signal at the wing-gear interface and compares this signal with the limit acceleration signal. The control is actuated when the wing-gear accelerometer signal exceeds the acceleration limit signal by a preset tolerance.

Figure 5 schematically illustrates three operational phases of the series-hydraulic active control gear during a landing impact. First, the gear contacts the runway at the measured sink rate and the shock-strut force builds as the strut stroking velocity $\dot{s}$ increases. The gear continues to operate in a passive mode (see fig. 5(a)) until the algebraic sum of the forces at the wing-gear interface (airplane weight, aerodynamic forces, and shock-strut force) exceeds the control limit force. The second operational phase occurs during shock-strut compression when the electronic control signals the servo valve to move the spool to connect the piston to the low-pressure accumulator. The rate at which the spool is moved is determined within the electronic control as a function of the stroking velocity of the shock strut. Hydraulic fluid will then flow from the shock-strut piston into the low-pressure accumulator (see fig. 5(b)) to limit the force rise in the shock strut. As the shock-strut velocity decreases, the shock-strut hydraulic force will decrease. If the wing-gear-interface acceleration drops below the limit acceleration and if the wing-gear-interface velocity is greater than a predetermined value, the rate of opening of the servo valve will be decreased to permit an increase of the hydraulic force and raise the shock-strut force. With continuing decrease in the shock-strut velocity and accompanying decrease in hydraulic force, the electronic control will command the servo valve spool to commence closing to maintain the wing-gear-interface acceleration within prescribed tolerances of the limit acceleration. When the servo valve spool returns to the fully closed position, the piston is isolated from the low-pressure accumulator. The third operational phase occurs as the wing-gear acceleration drops below the limit acceleration, and the electronic control commands the spool to connect the piston to the high-pressure hydraulic reservoir. Hydraulic fluid is then injected into the piston under high pressure to increase the hydraulic force. (See fig. 5(c).) The rate at which fluid is injected is determined by the rate of change of the shock-strut extension velocity.

The transition from the impact phase to the ground-roll phase is accomplished by linearly decreasing the limit-force signal from the value used during the impact phase to a value to be used during the ground-roll phase. During this transition, the limit acceleration tolerance will be increased to a value compatible with the active control gear design. With the assumption that the mass of the airplane remains constant during landing, the momentum of the wing-gear interface is determined by the wing-gear-interface velocity. The objective of the transition phase is to reset the signal for control limit acceleration and the tolerance signals to values compatible with a wing-gear-interface acceleration of zero for the ground-roll phase. This infers that the impact energy of the airplane has been dissipated. Transition to the ground-roll configuration is initiated when the wing-gear-interface velocity, which is continuously monitored by the electronic control, becomes equal to a signal input equivalent to an impulse divided by the airplane mass. For takeoff the control will be activated in the ground-roll mode. After takeoff, when the gear becomes fully extended, the control will be recycled into the impact phase of operation and will be deactivated during gear retraction. When the gear is extended for landing, the control will be activated in the impact mode.

Control effects are mathematically simulated by modifying the passive-gear shock-strut pressure equations, which are

Pneumatic

$$p_2 = p_{2,i}\left(\frac{V_{2,i}}{V_{2,i} - A_2 s}\right)^{\gamma} - p_{at}$$

Hydraulic

$$p_1 = \rho_H \left\{ \left[\frac{\left(A_1 - A_p\right)^2}{2C_{d,o}^2\left(A_o - A_p\right)^2} \right] \dot{s}^2 \frac{\dot{s}}{|\dot{s}|} \right\} + p_2$$

The principles used to modify the pressure equations are as follows: During shock-strut compression, the volume of incompressible fluid that normally would flow through the orifice in a small time interval is diverted to the low-pressure accumulator at a rate equivalent to the shock-strut compression rate and thus limits the hydraulic pressure increase. The modification of the passive-gear pressure equations for simulation of control effects is therefore based upon two control parameters: instantaneous volume flow rate into or from the piston and cumulative volume added to or removed from the piston. The pneumatic pressure is a function of the cumulative volume of fluid which has flowed from the piston to the control low-pressure accumulator or from the control high-pressure reservoir into the piston. Therefore, the equation for the pneumatic pressure incorporating active control is

$$p_2 = p_{2,i}\left(\frac{V_{2,i}}{V_{2,i} - A_2 s - V_{ac}}\right)^{\gamma} - p_{at}$$

The passive-gear shock-strut hydraulic pressure equation is modified to reflect control operation by solving for an effective shock-strut compression or extension velocity based on the control flow rate, the area of the piston, and the instantaneous shock-strut velocity as follows:

$$p_1 = \rho_H \left[\frac{(A_1 - A_p)^2}{2C_{d,o}^2 (A_o - A_p)^2} \left(\dot{s} + \frac{\dot{V}_{ac}}{A_1 - A_p} \right)^2 \frac{\dot{s} + \dfrac{\dot{V}_{ac}}{A_1 - A_p}}{\left| \dot{s} + \dfrac{\dot{V}_{ac}}{A_1 - A_p} \right|} \right] + p_2$$

The control flow rate and incremental values of flow are determined through an iterative process. These values of flow rate and flow are used in the pressure equation to solve for new values of pressure and shock-strut force. The following procedure is used to determine the flow rate and flow during strut compression: The shock-strut force was controlled to limit the force at the wing-gear interface during the preceding interval. The state of the integrated variables has been determined for this shock-strut force. The shock-strut force is recomputed on the basis of the updated variables and prior shock-strut and control parameters. If the shock-strut force results in a force at the wing-gear interface greater than the control limit force, the control must lower the shock-strut force. The updated hydraulic pressure and the control accumulator pressure are used to compute a temporary velocity of flow through the control line and servo valve:

$$v_{temp} = \left[\frac{2(p_H - p_{\ell c})}{\rho_H} \right]^{1/2}$$

This temporary velocity is then employed to compute the effective pressure p_{ec} between the piston and the control accumulator by introducing line losses:

$$p_{ec} = p_H - \frac{32\mu_H v_{temp} l_{c\ell}}{d_{c\ell}^2} - \gamma_H (z_\ell - s)$$

The effective velocity of flow for the instantaneous shock-strut parameters is defined as

$$v_{eff} = -\left[\frac{2(p_{ec} - p_{\ell c})}{\rho_H} \right]^{1/2}$$

The area of the servo valve opening required on the basis of the change in shock-strut velocity over the computing interval is determined as

$$A_{co}\big|_t = A_{co}\big|_{t-\Delta t} + \left|\frac{\Delta \dot{s}\left(A_1 - A_p\right)}{C_{d,co} v_{eff}}\right|$$

The control flow rate is defined as

$$\dot{V}_{ac}\big|_t = C_{d,co} A_{co}\big|_t v_{eff}$$

and the incremental flow occurring during the time interval is

$$\Delta V_{ac}\big|_t = \dot{V}_{ac}\big|_t \, \Delta t$$

The shock-strut force for the active gear is determined by the same equation used for the passive gear. If the shock-strut force again results in a wing force greater than the limit force, the control orifice area is increased and new values of flow rate and flow are computed on the basis of the shock-strut parameters at the beginning of the interval. The flow which occurred during the first iteration is removed from the cumulative flow and the new value of flow is algebraically summed. This iterative process continues until the wing force is within the design tolerance of the control limit force. Mathematical simulation of flow from the control high-pressure reservoir into the shock-strut piston is accomplished in a similar manner.

Elastic-Wing Model

Limited structural-flexibility effects are considered by including in the mathematical model first-mode wing bending and wing torsional characteristics. The wing bending mode is defined as the deflection of the elastic axis of the wing deforming as a cantilever beam. The wing mass, wing-gear interface, and engine mass are assumed to be located on the wing chord at the same spanwise location. The wing is also assumed to be rectangular in planform. The equation for the spanwise bending spring constant may, with the foregoing assumptions, be expressed as

$$K_{wB} = \frac{3EI_{sect}}{y^3}$$

The bending deflection z_{Be} of the wing is determined from the relative motion of the intersection of the wing elastic axis with the X_b-Z_b plane containing the fuselage center line and the wing elastic axis at the spanwise chord containing the wing mass center. The wing bending force is determined from the product of wing bending deflection and the wing bending spring constant:

$$F_{wB} = K_{wB} z_{Be}$$

The first-mode torsional characteristics of the wing are determined assuming a constant wing cross section from the fuselage center line to the spanwise chord containing the wing mass center and the wing-gear interface. Wing torsional deflection is assumed to occur about the elastic axis and the wing chord is assumed to remain undeformed. With these assumptions the wing torsional spring constant is

$$K_{w\mathcal{T}} = 2.0 S_{sect}^{2} \frac{G}{y}\left(\frac{h}{t_{wbv}} + \frac{w_{wbx}}{t_{wbh}}\right)$$

where

S_{sect}	chordwise area of wing cross section, m^2 (ft^2)
y	spanwise distance from fuselage center line to chord containing wing-gear interface, m (ft)
h	height of wing box, m (ft)
t_{wbh}	thickness of horizontal wing box units, m (ft)
t_{wbv}	thickness of vertical wing box units, m (ft)
w_{wbx}	width of wing box, m (ft)

The torsional elastic deformation α_e of the wing chord at the spanwise location of the wing mass center relative to the wing chord at the fuselage center line is determined from the relative angular motion of these sections. The wing torque is defined as the product of the torsional elastic deformation and the wing torsional spring constant:

$$M_{ew} = K_{w\mathcal{T}} \alpha_e$$

Aerodynamic Model

The aerodynamic model employed is based on theoretical subsonic aerodynamics, neglecting ground effects, determined from reference 8. The theoretical lift-curve slope for a wing of infinite aspect ratio is

$$a_\infty = dC_L/d\alpha = 2\pi \text{ per radian}$$

For a finite aspect ratio, the lift-curve slope is approximately

$$a = \frac{a_\infty}{1 + \frac{2}{AR}} \text{ per radian}$$

The wing lift force is

$$L_W = 0.5\rho_a S_W \dot{x}_{c,g}^2 C_L$$

where

$$C_L = a\left(\theta + \alpha + \tan^{-1} \frac{\dot{z}_{c,g}}{\dot{x}_{c,g}}\right)$$

The tail lift force is found in a similar manner.

The wing aerodynamic drag force (ref. 8) is assumed to consist of induced drag, friction drag, and profile drag and is defined as follows:

$$D_W = 0.5\rho_a S_W \dot{x}_{c,g}^2 (C_{D,i} + C_{D,f} + C_{D,p})$$

where

Induced drag,

$$C_{D,i} = \frac{C_L{}^2 S_W}{\pi AR}$$

Friction drag,

$$C_{D,f} = 0.0375(N_{Re})^{-0.15}$$

Profile drag,

$$c_{D,p} = 0.075\left(N_{Re}\right)^{-0.15}$$

The drag forces for the tail surfaces and the fuselage are determined in a similar manner.

EQUATIONS OF MOTION

The deterministic solution consists of determining the forces to be used in the equations of motion, defining the coupled equations of motion which govern the response of the airplane, and performing numerical integration of the equations of motion on a digital computer. The equations of motion were written for two separate options: rigid-airframe option, and rigid-fuselage—elastic-wing option. The coupled equations of motion are presented in appendix A for both options.

For the elastic wing, the wing mass center has additional degrees of freedom, which are perturbations in the Z_b-direction and in rotation about the elastic axis relative to the rigid-body motions of the airplane.

The equations of motion were solved by performing a numerical integration. The numerical integration procedure is based on the classical fourth-order Runge-Kutta formula, and use of Richardson's extrapolation-to-the-limit theory results in a fifth-order integration procedure. This procedure operates with a variable time interval which is sized to meet a specified local relative truncation error.

ANALYTICAL MODEL SIMULATIONS

To validate the mathematical model described in the foregoing sections and to perform an evaluation of the active-control gear, a landing-gear and airplane configuration was modeled to permit simulations of vertical-drop tests, landing impacts, and landing roll-outs with the ACOLAG computer program. To accommodate the active control, the passive gear was modified in the analysis to provide additional stroke capability. The stroke was increased from 0.187 m (7.375 in.) to 0.264 m (10.375 in.) by increasing the cylinder length, pneumatic volume, and piston length.

Passive Gear

Vertical-drop test.- To permit comparison between computed data from the ACOLAG computer program with experimental drop-test data, the program was adapted to include tire hysteresis for the nonrotating wheel (ref. 3), and braking simulation was excluded. A lumped mass at the gear trunnion was used to simulate a rigid airframe. The passive landing gear (ref. 7) from a 2268-kg (5000-lbm) class airplane was selected, since experimental vertical-drop-test data were available for this gear. A sketch of the shock strut and the geometric characteristics of the gear are presented in appendix B. The impact parameters were a sink rate of 2.7 m/sec (8.8 ft/sec); a lift force of 10.7 kN (2412.5 lbf), which was held constant throughout the impact; a pitch angle of 0° (gear normal to impact surface); and a wheel rotational velocity of 0 rad/sec (0 ft/sec).

Landing impact. - For comparison of computed data with data obtained from transversely symmetrical airplane landings, tire hysteresis effects were eliminated (ref. 3) and antiskid braking was included. An airplane configuration was defined in terms of geometry, a rigid-airframe lumped mass distribution, and aerodynamics compatible with the selected landing gear. The geometry and lumped mass distribution of the airplane configuration are shown schematically in figure 6.

Since experimental landing-impact data are not available for the selected passive gear (ref. 7), ACOLAG was evaluated for landing impact by comparing the results of this simulation with computed results obtained from a multiple-degree-of-freedom takeoff and landing analysis (TOLA), which, as described in reference 9, will only accommodate conventional gears and a rigid airframe. The impact parameters were a sink rate of 2.7 m/sec (8.8 ft/sec); a ground speed of 45.7 m/sec (150 ft/sec); a pitch angle of 10.5°; an angle of attack of 13.8°, which results in a lift force equal to the airplane weight at touchdown; and a wheel rotational velocity of 0 rad/sec (0 ft/sec).

Landing roll-out. - To determine the damping characteristics of the modified passive gear, a landing roll-out simulation was made. For this simulation the airplane was placed on the runway with a pitch angle of 0 rad (0 deg), the gear and tire deflected to support the mass of the airplane, the tire and wheel in the free-rolling condition, and a ground speed equal to 44.5 m/sec (146 ft/sec). The simulation was started with the tire encountering a sinusoidally varying (3 Hz with a half-amplitude of 0.0254 m (0.0833 ft)) runway bump which had an initial elevation of zero. At the end of one-quarter cycle, the surface was dropped vertically to zero elevation and remained at this elevation for the remainder of the simulated roll-out.

Active Gear

Vertical-drop test. - No experimental data are available for the active control gear. Therefore, evaluation of the active control gear was accomplished by comparing computed results for the active gear with those of the passive gear for the vertical-drop test. The gear parameters and impact parameters were the same as those for the passive gear.

Landing impact. - For this case evaluation of the active control gear was accomplished by comparing computed results for the active gear with those of the modified passive gear. The airplane configuration and impact parameters were the same as those described in the section "Landing impact" for the passive gear.

Landing roll-out.- To compare the damping characteristics of the active gear with those of the modified passive gear, a landing roll-out simulation was made for the airplane and runway parameters cited in the section "Landing roll-out" for the passive gear.

The modification of the passive gear discussed in this paper is simply an expedient method to characterize the range of control parameters that would be required for such a design. However, it should be noted that an active control gear would not be a simple modification of a passive-gear design, but would require an independent design based upon optimization of gear parameters in conjunction with control parameters.

RESULTS AND DISCUSSION

To evaluate the ACOLAG computer program, results were obtained from the vertical-drop-test simulation and compared with the experimental data reported in reference 7. The TOLA computer program (ref. 9) was also employed to simulate the same vertical-drop test and the results were compared with the experimental data. Evaluation of the ACOLAG landing-impact simulation was accomplished by comparing results obtained by using the rigid-airframe and passive-gear modes with results obtained for a similar calculation employing the TOLA computer program.

Results are presented for vertical-drop-test simulations with stationary and vertically oscillating impact surfaces; for landing-impact simulations on a flat runway surface and a sinusoidally varying amplitude surface; and for a landing roll-out on a runway surface having a single, quarter-cycle, sinusoidal bump ending in a vertical discontinuity at peak amplitude, followed by a flat surface.

Passive Gear

Vertical-drop simulations.- Figure 7(a) presents computed and experimental time histories of shock-strut force and stroke during the impact phase of the vertical-drop test of the passive gear. Since rebound of the upper mass (airframe mass) occurred at approximately 0.16 sec in both the experiment (ref. 7) and the computer simulation, data are not presented beyond this time. The shock-strut forces computed from ACOLAG and TOLA are in excellent agreement and both are in good agreement with the experimental data. As was the case with the shock-strut force, the calculated shock-strut strokes for the two programs are in excellent agreement and both are in good agreement with the experimentally determined strokes for most of the time history.

Time histories of vertical ground force and tire deflection, computed for a rigid airframe and a passive gear, are compared in figure 7(b) with experimental data obtained from the vertical-drop test (ref. 7). Computed vertical ground forces are generally in excellent agreement with the ground force obtained from the experiment. The ground force computed from the ACOLAG program is in excellent agreement with that computed from the TOLA program. The tire deflections calculated from the ACOLAG program are in excellent agreement with those computed from the TOLA program and both are in good agreement with experimental data.

Figure 7(c) presents a comparison of mass-center accelerations (nomenclature for experimental data is upper-mass accelerations) for the computed results and experimental data. Since the shock-strut force is the only varying force applied to the upper mass, the trend of the comparison should be the same as that for the shock-strut force (fig. 7(a)). The trend is the same and the agreement between computed and experimental mass-center accelerations is good.

Landing-impact simulations.- Evaluation of the ACOLAG computer program for the landing-impact option is accomplished by comparing computed results from the ACOLAG program with results from the TOLA program. These comparisons are presented in figure 8.

Time histories of pitch attitude are compared in figure 8(a) for a landing impact on a flat runway. The agreement between the computed results from the two programs is excellent.

Time histories of shock-strut force and stroke calculated from the two programs are compared in figure 8(b). The shock-strut forces are in excellent agreement. Although the shock-strut strokes computed from the ACOLAG program are slightly less than those calculated from the TOLA program, the agreement is good.

Computed time histories of vertical ground force and tire deflection are compared in figure 8(c). The vertical ground forces and tire deflections calculated with the ACOLAG program are in good agreement with those computed with the TOLA program.

Airplane mass-center accelerations obtained from the ACOLAG and TOLA programs are compared in figure 8(d). The Z_b-axis accelerations are in good agreement to a time of approximately 0.17 sec. At this time, the TOLA program indicates that the nose gear has contacted the surface, and hence the Z_b-axis accelerations increase. The ACOLAG program has the nose gear contacting the surface at a time of approximately 0.18 sec, at which time, because of the simplified nose-gear representation, data from the ACOLAG program are not comparable with those of the TOLA program. Mass-center X_b-axis accelerations are in good agreement to a time of approximately 0.11 sec. At this time the wheel has spun up and is in a free-rolling state. When the wheel is freely rolling, the tire-runway friction coefficient in ACOLAG is decreased to a value which produces no wheel slippage. This tire-runway friction coefficient resulted in a very small component of ground drag force applied at the mass center, while the X_b-axis component of the vertical ground force was sufficiently large to develop a positive X_b-axis acceleration of the mass center. The definition of the tire-runway friction coefficient in TOLA resulted in a larger tire-runway friction coefficient during free rolling of the wheel. Consequently, the ground drag force applied at the mass center and hence the mass-center X_b-axis accelerations were greater. Comparison of X_b-axis accelerations was also terminated at the time of contact between the nose gear and the surface.

Considering the good agreement shown between TOLA and ACOLAG results when compared with experimental data and when compared with each other, the ACOLAG program appears to be a valid tool for the study of various actively controlled landing gears.

Series-Hydraulic Active Control Landing Gear

Results which demonstrate the operation of a series-hydraulic active control gear for vertical-drop and landing-impact simulations are presented and compared in figures 9 to 13.

Vertical-drop simulations.- Computed results for the passive and active control gears are compared in figure 9 for a vertical drop onto a flat stationary surface. Figure 9(a) presents a comparison between the wing forces experienced during a vertical-drop simulation of the passive and active gears. The wing force is shown as a function of wing displacement. Presentation of the active-gear results is discontinued at the maximum value of wing displacement because in the vertical-drop simulation the aerodynamic lift was maintained constant at a value equivalent to the mass of the airplane, and hence results calculated during rebound are not physically realistic for a landing simulation. For the active-gear simulation the wing force was limited to 21.46 kN ± 334 N (4825 lbf ± 75 lbf), which represents a 26-percent reduction from that of the passive-gear simulation.

It was noted in reference 2 that for aluminum structures undergoing a cyclical level resulting in a fatigue life of approximately 10^5 cycles, the relation between the number of cycles to failure N and peak-to-peak stress σ is

$$N = A/\sigma^5$$

where $A = 1.8 \times 10^{27}\ \mathrm{Pa}^5\ (\mathrm{lbf}^5/\mathrm{ft}^{10})$. If a fully reversed stress of 241 $\mathrm{MN/m^2}$ (35 000 psi) for the passive gear simulation is assumed on an aluminum wing structure, the fatigue life of this structure would be 34 000 cycles. With the wing force controlled to a value of 74 percent of the passive-gear value, the same structure would have an increased fatigue life of approximately 4.5 times, or 154 000 cycles. Thus it appears that small reductions in cyclical stress levels have a significant effect on the fatigue life of the structure. Reduction in wing force, however, results in an increase in wing displacement of approximately 10 percent for this case, which is primarily reflected in an increased shock-strut stroke. For energy compatibility to exist between the passive-gear and the active-gear simulations, the hatched areas of figure 9(a) must be equal. The energies represented by the hatched areas were determined to be nearly the same. Thus, the incorporation of the control analysis into the passive-gear analysis results in an energy-compatible procedure, which increases confidence in the validity of active control landing gear analysis.

Time histories of shock-strut force and stroke for the passive and active gears are compared in figure 9(b). At approximately 0.047 sec, control of the shock-strut force level at 21.46 kN ± 334 N (4825 lbf ± 75 lbf) was initiated to maintain the wing force within the preset limits, which were exceeded at this time. Since the strut was compressing, the control removed fluid and the maximum flow rate attained was -428 ℓ/min (-113 gal/min) at 0.084 sec. A transfer from the low-pressure mode to the high-pressure mode was required at 0.11 sec to maintain the wing force. This transfer results in a shift to the lower bound of the control limit force and accounts for the lower shock-strut force during the time from 0.11 sec to 0.143 sec. The maximum injection flow rate of 458 ℓ/min (121 gal/min) occurred at a time of 0.129 sec. The momentum of the upper mass becomes equal to the impulse designed into the electronic control circuit at a time of 0.143 sec, and the electronic control commands a linear decrease in the limit force from the impact limit force to the roll-out limit force. When the roll-out limit force is reached, data presentation is terminated. At the time of initiation of control at the roll-out limit force (0.18 sec), the shock-strut stroke for the active-gear simulation was approximately 17 percent greater than the stroke shown for the passive-gear simulation.

Figure 9(c) shows calculated time histories of vertical ground force and tire deflection for the vertical-drop simulations of the passive and active gears. As would be expected for the controlled lower shock-strut force, both the vertical ground force and tire deflection were lower for the active-gear simulation than those for the passive-gear simulation.

Computed results for the passive and active control gears are compared in figure 10 for a vertical drop onto a vertically oscillating surface. The vertically oscillating surface was introduced to simulate a sinusoidally varying runway-unevenness effect, since no ground speed is involved with vertical-drop testing. The surface oscillation, a frequency of 10 Hz and a half-amplitude of 0.0254 m (0.0833 ft), was selected as a worse-case condition, since this corresponded to the resonant frequency of the hub mass. At touchdown the surface was set into an upward motion opposite to that of the gear.

Wing force as a function of wing displacement is shown in figure 10(a) for the vertical-drop simulation. In the initial phase of this simulation the ground motion passed through the peak displacement and was moving away from the tire. The resulting initial rise in wing force did not exceed the upper bound of the limit force (21.80 kN (4900 lbf)); consequently, the control was not activated. During the fourth quarter of the first cycle of ground motion, however, the control was activated because the ground was again moving into the tire and the resulting wing force exceeded the upper bound of the control limit force. The wing force, for the active gear in this simulation, attained a value of only 64 percent of that of the passive gear with an increase in wing displacement of only 5 percent.

Time histories of shock-strut force and stroke are shown in figure 10(b) for the vertical-drop simulation with the oscillating surface. The appreciable reduction in wing force (36 percent) with the relatively small increase in wing displacement (5 percent), as shown in figure 10(a), was not attained without penalty. To achieve these values, the maximum control flow rates required, as shown in figure 10(b), were -723 ℓ/min (-191 gal/min) during compression and 1423 ℓ/min (376 gal/min) during transition from impact to roll-out control. Also, a 25-percent increase in shock-strut stroke above that of the passive gear was required. However, it should be recalled that the surface motion was chosen to create a worse-case condition, and for this study the gear was not optimized to be compatible with the series-hydraulic control.

Figure 10(c) shows time histories of vertical ground force and tire deflection computed for this simulation. As would be expected, the maximum ground force and tire deflection for the active gear were smaller than those computed for the passive gear during the portion of the impact phase prior to rebound.

Landing-impact simulations.- Comparisons of computed data for the modified passive gear and the series-hydraulic active control gear are presented in figures 11 and 12. Figure 11 shows comparisons of computed data for landing-impact simulations onto a smooth runway. Comparisons of computed data for landing-impact simulations onto a sinusoidally uneven runway (frequency of 10 Hz with a half-amplitude of 0.0254 m (0.0833 ft)) are shown in figure 13.

Figure 11(a) presents comparisons of computed wing force as a function of wing displacement for the passive gear and the active gear. The active gear achieved a 20-percent reduction in wing force relative to the passive gear, with an increase in wing displacement of 8 percent.

Figure 11(b) compares computed time histories of shock-strut force and stroke for the passive and active gears. The shock-strut force for the active control gear gradually increases during the initial control phase, in contrast to the essentially constant shock-strut force for the vertical-drop simulation. (See fig. 9(b).) Since the wing force is the force being maintained by the control, the shock-strut force increases to offset the decrease in lift force as the airplane pitches down during the impact. The maximum control flow rates required during this simulation were 447 ℓ/min (118 gal/min) for injection of fluid into the piston and -397 ℓ/min (-105 gal/min) for removal of fluid from the piston.

At the time of nose gear contact (0.18 sec), the shock-strut stroke of the active gear was 25 percent greater than that of the passive gear.

Time histories of vertical ground force and tire deflection are shown in figure 11(c). Again, the maximum vertical ground force and tire deflection for the active gear were less than those of the passive gear during the impact phase.

Figure 12 presents time histories of control flow rate and control flow which were required during the landing-impact simulation on a smooth runway. Following control initiation, the control removed fluid from the strut and attained a maximum flow rate of approximately -360 ℓ/min (-95 gal/min). The flow rate decreased from this maximum value to zero at a time of 0.098 sec, which indicates that the control required a transition from the low-pressure mode of operation to the high-pressure mode at this time. The flow rate increased in the high-pressure mode to a value of 447 ℓ/min (118 gal/min) at a time of 0.118 sec. At a time of 0.12 sec (see fig. 11(b)), the control initiated the transition from the impact control limit force to the roll-out control limit force. During this transition, the control required a shift from the high-pressure mode of operation to the low-pressure mode at a time of approximately 0.139 sec. Fluid was then bled from the piston and reached a maximum flow rate of approximately -397 ℓ/min (-105 gal/min). The flow rate decreased from this maximum until, at a time of 0.18 sec, the nose gear contacted the surface and the results were terminated.

The control flow shown in this figure is the cumulative volume of fluid removed or injected into the piston at any instant of time. During the initial low-pressure mode of operation, approximately 0.156 ℓ (0.0055 ft^3) of fluid was removed from the strut. This occurred at a time of 0.098 sec, where the transition from the low-pressure mode to the high-pressure mode of operation occurred. Fluid was then injected into the strut until the second operational transition occurred at a time of 0.139 sec. At this time all the fluid that had been removed from the strut had been returned and an additional amount of approximately 0.0255 ℓ (0.0009 ft^3) had been injected into the strut. Fluid was again removed from the strut, and at the time of nose-gear contact with the surface (0.18 sec), approximately 0.130 ℓ (0.0046 ft^3) had been removed. Consequently, after the impact phase, the fluid remaining in the gear was approximately 92 percent of the fluid in the gear prior to touchdown.

Comparisons of computed results for the simply modified passive gear and the series-hydraulic control version of this gear are shown in figure 13 for a landing-impact simulation onto an extremely uneven, sinusoidally varying runway surface. Figure 13(a) presents wing force as a function of wing displacement. As in previous cases, the computed results show that the active control analysis is an energy-compatible procedure.

Figure 13(b) shows time histories of shock-strut force and stroke for the landing impact onto the sinusoidally varying runway surface. The versatility of the active control logic of the analysis may be seen by comparing the shock-strut-force results shown in this figure with those shown in figure 10(b) at the time of control activation. As discussed in connection with the vertical-drop simulation, control activation was initiated in the low-pressure phase, as anticipated during development of the control logic, and occurred during the fourth quarter of the first cycle of surface oscillation. In figure 13(b) control was initiated in the low-pressure phase during the first one-quarter cycle of surface oscillation; however, the next one-half cycle of the surface oscillation was in phase with the wing motion and the shock-strut force for the passive gear decreased. As a consequence, the wing force decreased below the lower tolerance of the wing limit force and the high-pressure phase was required to maintain the wing force within the limits. Operation remained in the high-pressure phase until transition was required from the impact control limit force to roll-out control limit force. Since no experimental data are available on active control landing gears, this illustration of the versatility of the control logic in dealing with unexpected interactive effects increases confidence in the active control landing gear analysis.

The maximum control flow rates encountered in this simulation were 432 ℓ/min (114 gal/min) for the high-pressure phase of operation and -1154 ℓ/min (-305 gal/min) for the low-pressure phase of operation. These large flow rates coupled with tire bounce (see fig. 13(b)) are undesirable.

Time histories of vertical ground force and tire deflection for this simulation are presented in figure 13(c). The computed results for the active control gear show that upon control activation, ground force and tire deflection become greater than those for the passive gear. As previously noted in figure 13(a), the wing force for the passive gear is oscillatory because of the runway perturbations. It is desirable from the standpoint of fatigue not only to limit the magnitude of the forces applied to the upper body but to reduce oscillations as well. Consequently, with the control operating in the high-pressure mode the shock-strut force was increased to prevent the wing-force oscillation. As a result of this increased shock-strut force, the ground force and tire deflection increased relative to those obtained for the passive gear. Presentations of active-gear results are discontinued at the time the tire leaves the surface.

Landing roll-out simulations.- The effects of the series-hydraulic control on the damping characteristics of the modified oleo-pneumatic shock strut are shown in figure 14 by comparing time histories of wing force and vertical ground force for the active and passive gears during a roll-out simulation. The simulations were made assuming that the mass of the airplane was supported by the main gears and the ground speed was 44.5 m/sec (146 ft/sec).

Figure 14(a) presents computed time histories of wing force for the passive and active gears for the roll-out simulation. For the active gear, the wing force was controlled about zero force with a tolerance of ±2134 N (±480 lbf) and the wing force varied from zero to approximately -3114 N (-700 lbf). At a time of approximately 0.08 sec the runway elevation dropped vertically to zero and the wing force for the passive gear increased very rapidly to a value of 4782 N (1075 lbf). At a time of 2 sec, the wing force for the passive gear had damped to about 11 percent of the peak-to-peak value encountered during the first cycle. The active-gear simulation shows that the series-hydraulic control limited the wing force to the control limit force during the first two cycles, and at a time of 2 sec, the wing force had damped to about 5 percent of the peak-to-peak value encountered during the first two cycles.

Computed time histories of vertical ground force are presented in figure 14(b) for both the passive- and active-gear landing roll-out simulations. The peak-to-peak excursion of vertical ground force for the active gear, after the surface discontinuity, was greater than that for the passive gear. Subsequent peak-to-peak force oscillations, about the static ground force of 10.7 kN (2412.5 lbf), were lower than those of the passive gear.

On the basis of these comparisons of wing force and vertical ground force for both the passive and active gears, it appears that the damping characteristics of the series-hydraulic active control gear were equivalent to or better than those of the modified passive gear for an excitation resulting from a vertically discontinuous, sinusoidal bump. In addition, the wing force encountered during traverse of the bump was reduced by 30 percent of the wing force experienced by the passive gear.

CONCLUDING REMARKS

A mathematical model of an active control landing gear has been developed and programed for operation on a digital computer. The principles upon which the model is based have also been discussed. The model has been evaluated for predicting airplane loads and motions encountered during simulations of a vertical drop and a landing impact of a rigid airframe with a landing gear incorporating a conventional (passive) oleo-pneumatic shock strut. Results have also been presented for the operation of a series-hydraulic active control gear for similar simulations of a vertical drop and landing impact and roll-out.

The results obtained from this investigation are summarized in the following statements: The computed results from the subject mathematical model, simulating a vertical-drop test with a rigid airframe and a passive gear, are in good agreement with experimental data and with results obtained from a multiple-degree-of-freedom takeoff and landing analysis (TOLA). Computed results for a landing-impact simulation, with a rigid airframe and passive gear, are in excellent agreement with results computed for the same landing-impact simulation employing TOLA. On the basis of these comparisons, it appears that the mathematical model of the active control landing gear is valid for the prediction of airplane landing loads and motions for simulated symmetrical landings of a rigid airframe with passive main landing gears.

Results of vertical-drop and landing-impact simulations employing the mathematical model of the active control landing gear show that wing forces, relative to those encountered with the modified passive gear, can be reduced substantially during the impact phase of the landing. The vertical-drop simulation for the active gear resulted in limiting the wing force to 75 percent of the force for the modified passive gear with a 15-percent increase in shock-strut stroke. The results of the landing-impact simulation for the active gear on a smooth runway indicated that the wing force could be limited to 80 percent of the force for the modified passive gear during the impact phase, with a 25-percent increase in strut stroke relative to that encountered during passive-gear simulation. The results for a landing-impact simulation onto an extremely uneven runway also indicated that the wing force could be limited, during the impact phase, to 80 percent of the wing force encountered with the modified passive gear. In this case, however, a 45-percent increase in shock-strut stroke relative to that encountered with the passive gear was required. These reductions in wing force could result in substantial increases in fatigue life of the structure.

Comparison of computed results for the active and passive gears during a landing roll-out, in which the gears were forced into motion by a single, discontinuous, one-quarter cycle, sinusoidal bump, indicated that the series-hydraulic active control gear had damping characteristics equivalent to or slightly better than those inherent in the modified passive gear. For these simulations, the active gear reduced the wing force by 30 percent of the wing force generated by the passive gear.

Control flow rates required by some of these simulations were very large and, if ultimately required for this type of active control gear, could necessitate advances in servo valve technology. However, it should be reemphasized that these results were for a simply modified version of a landing gear with a conventional oleo-pneumatic shock strut and, consequently, do not necessarily represent optimum results that could be obtained with a gear specifically designed to be compatible with the series-hydraulic control concept.

Langley Research Center
National Aeronautics and Space Administration
Hampton, Va. 23665
December 18, 1975

APPENDIX A

EQUATIONS OF MOTION

This appendix presents the equations of motion for the physical system shown schematically in figures 3 and 4 for the rigid-airframe option and the rigid-fuselage—elastic-wing option.

Rigid-Airframe Option

The equations of motion for the rigid-airframe option in the body-axis system and the gravity-axis system are presented in this section.

Airplane center-of-gravity (composite mass center) motion in body-axis system

$$\ddot{x}_{c,b} = \frac{\begin{bmatrix} 0.5L_t \sin\alpha - 0.5(D_f + D_t)\cos\alpha - 0.5D_w + F_{G,X}\cos(\theta + \alpha) - F_{G,Z}\sin(\theta + \alpha) \\ - (m_f + m_w + m_h)g \sin(\theta + \alpha) \end{bmatrix}}{m_f + m_w + m_h}$$

$$\ddot{z}_{c,b} = \frac{-0.5L_w - 0.5L_t \cos\alpha - 0.5(D_f + D_t)\sin\alpha - F_{A,ss} + (m_f + m_w)g\cos(\theta + \alpha)}{m_f + m_w}$$

Airplane center-of-gravity motion in gravity-axis system

$$\ddot{x}_{c,g} = \ddot{x}_{c,b}\cos(\theta + \alpha) + \ddot{z}_{c,b}\sin(\theta + \alpha)$$

$$\ddot{z}_{c,g} = \ddot{z}_{c,b}\cos(\theta + \alpha) - \ddot{x}_{c,b}\sin(\theta + \alpha)$$

Hub motion in body-axis system

$$\ddot{x}_{h,b} = \ddot{x}_{c,b} + \ddot{\theta}d_2 + \dot{\theta}^2 d_1 - 2\dot{\theta}\dot{s}$$

$$\ddot{z}_{h,b} = \frac{F_{G,Z}\cos(\theta + \alpha) + F_{G,X}\sin(\theta + \alpha) + F_{A,ss} + m_h g\cos(\theta + \alpha)}{m_h}$$

APPENDIX A

Hub motion in gravity-axis system

$$\ddot{x}_{h,g} = \ddot{x}_{h,b} \cos (\theta + \alpha) + \ddot{z}_{h,b} \sin (\theta + \alpha)$$

$$\ddot{z}_{h,g} = \ddot{z}_{h,b} \cos (\theta + \alpha) - \ddot{x}_{h,b} \sin (\theta + \alpha)$$

Wing-mass-center motion in gravity-axis system

$$\ddot{x}_{w,g} = \ddot{x}_{c,g} + \ddot{\theta} d_{cw} \sin (\lambda_{cw} + \theta) + \dot{\theta}^2 d_{cw} \cos (\lambda_{cw} + \theta)$$

$$\ddot{z}_{w,g} = \ddot{z}_{c,g} + \ddot{\theta} d_{cw} \cos (\lambda_{cw} + \theta) - \dot{\theta}^2 d_{cw} \sin (\lambda_{cw} + \theta)$$

Fuselage-mass-center motion in gravity-axis system

$$\ddot{x}_{f,g} = \ddot{x}_{c,g} - \ddot{\theta} d_{cf} \sin (\lambda_{cf} + \theta) - \dot{\theta}^2 d_{cf} \cos (\lambda_{cf} + \theta)$$

$$\ddot{z}_{f,g} = \ddot{z}_{c,g} - \ddot{\theta} d_{cf} \cos (\lambda_{cf} + \theta) + \dot{\theta}^2 d_{cf} \sin (\lambda_{cf} + \theta)$$

Wing-gear-interface motion in gravity-axis system

$$\ddot{x}_{wG,g} = \ddot{x}_{c,g} + \ddot{\theta} d_{cwG} \sin (\lambda_{cwG} + \theta) + \dot{\theta}^2 d_{cwG} \cos (\lambda_{cwG} + \theta)$$

$$\ddot{z}_{wG,g} = \ddot{z}_{c,g} + \ddot{\theta} d_{cwG} \cos (\lambda_{cwG} + \theta) - \dot{\theta}^2 d_{cwG} \sin (\lambda_{cwG} + \theta)$$

Shock-strut motion in body-axis system

$$\ddot{s}_b = \ddot{z}_{wG,g} \cos (\theta + \alpha) + \ddot{x}_{wG,g} \sin (\theta + \alpha) - \ddot{z}_{h,g} \cos (\theta + \alpha) - \ddot{x}_{h,g} \sin (\theta + \alpha) - \dot{\theta}^2 l_{ss}$$

Pitch angular acceleration about airplane center of gravity

$$\ddot{\theta} = \frac{\left[\begin{array}{l} -0.5L_t d_{ct} + 0.5D_f d_{cf} + 0.5D_t d_{ct} + 0.5L_w d_{cw,x} \cos \alpha - 0.5L_w d_{cw,z} \sin \alpha \\ - 0.5D_w d_{cw,z} \cos \alpha - 0.5D_w d_{cw,x} \sin \alpha - F_{A,ss} d_1 + F_{G,X} d_2 \cos (\theta + \alpha) \\ - F_{G,Z} d_2 \sin (\theta + \alpha) + M_n \end{array}\right]}{I_{YY}}$$

Wheel angular acceleration about hub

$$\ddot{\phi} = \frac{M_a + M_{br}}{I_a}$$

Brake-control sensor-mass acceleration about hub

$$\ddot{\beta} = 2\omega_{n,\beta} \frac{C_\beta}{C_{\beta,cr}} (\dot{\phi} - \dot{\beta}) + \omega_{n,\beta}^2 (\phi - \beta)$$

Rigid-Fuselage—Elastic-Wing Option

The equations of motion for the rigid-fuselage—elastic-wing option in the body-axis system and the gravity-axis system are presented in this section.

Airplane center-of-gravity (composite mass center) motion in body-axis system

$$\ddot{x}_{c,b} = \frac{\left[\begin{array}{l} 0.5L_t \sin \alpha - 0.5(D_f + D_t) \cos \alpha - 0.5D_w + F_{G,X} \cos (\theta + \alpha) - F_{G,Z} \sin (\theta + \alpha) \\ - (m_f + m_w + m_h)g \sin (\theta + \alpha) \end{array}\right]}{m_f + m_w + m_h}$$

$$\ddot{z}_{c,b} = \frac{-0.5L_t \cos \alpha - 0.5(D_f + D_t) \sin \alpha - F_{wB} + m_f g \cos (\theta + \alpha) - F_n \cos \theta}{m_f}$$

Airplane center-of-gravity motion in gravity-axis system

$$\ddot{x}_{c,g} = \ddot{x}_{c,b} \cos (\theta + \alpha) + \ddot{z}_{c,b} \sin (\theta + \alpha)$$

$$\ddot{z}_{c,g} = \ddot{z}_{c,b} \cos (\theta + \alpha) - \ddot{x}_{c,b} \sin (\theta + \alpha)$$

Hub motion in body-axis system

$$\ddot{x}_{h,b} = \frac{\left[\begin{array}{l} F_{G,X} \cos (\theta + \alpha) - F_{G,Z} \sin (\theta + \alpha) \\ - (m_f + m_w + m_h)g \sin (\theta + \alpha) - 0.5D_w \\ - 0.5(D_f + D_t) \cos \alpha + 0.5L_t \sin \alpha \end{array}\right]}{m_f + m_w + m_h} + \ddot{\alpha} d_{eh} \cos \lambda_{eh} + \dot{\alpha}^2 d_{eh} \sin \lambda_{eh}$$

$$+ \ddot{\theta} d_{ce} \sin \lambda_{ce} - \dot{\theta}^2 d_{ce} \sin \lambda_{ce}$$

APPENDIX A

Prior to shock-strut stroking

$$\ddot{z}_{h,b} = \frac{\left[\begin{array}{l} F_{G,Z} \cos(\theta + \alpha) + F_{G,X} \sin(\theta + \alpha) \\ + (m_w + m_h) g \cos(\theta + \alpha) - 0.5L_w + F_{wB} \end{array}\right]}{m_w + m_h} + \ddot{\alpha} d_{eh} \sin \lambda_{eh} - \dot{\alpha}^2 d_{eh} \cos \lambda_{eh}$$

Subsequent to shock-strut stroking

$$\ddot{z}_{h,b} = \frac{F_{A,ss} + F_{G,Z} \cos(\theta + \alpha) + F_{G,X} \sin(\theta + \alpha) + m_h g \cos(\theta + \alpha)}{m_h}$$

Hub motion in gravity-axis system

$$\ddot{x}_{h,g} = \ddot{x}_{h,b} \cos(\theta + \alpha) + \ddot{z}_{h,b} \sin(\theta + \alpha)$$

$$\ddot{z}_{h,g} = \ddot{z}_{h,b} \cos(\theta + \alpha) - \ddot{x}_{h,b} \sin(\theta + \alpha)$$

Wing-mass-center motion in body-axis system

$$\ddot{x}_{w,b} = \frac{\left[\begin{array}{l} F_{G,X} \cos(\theta + \alpha) - F_{G,Z} \sin(\theta + \alpha) \\ - (m_f + m_w + m_h) g \sin(\theta + \alpha) - 0.5F_{wB} \\ - 0.5(D_f + D_t) \cos \alpha + 0.5L_t \sin \alpha \end{array}\right]}{m_f + m_w + m_h} + \dot{\alpha} d_{ew} + \ddot{\theta} d_{ce} \sin \lambda_{ce} - \dot{\theta}^2 d_{ce} \cos \lambda_{ce}$$

Prior to shock-strut stroking

$$\ddot{z}_{w,b} = \frac{\left[\begin{array}{l} F_{G,Z} \cos(\theta + \alpha) + F_{G,X} \sin(\theta + \alpha) + (m_w + m_h) g \cos(\theta + \alpha) \\ -0.5L_w + F_{wB} \end{array}\right]}{m_w + m_h} + \ddot{\alpha} d_{ew}$$

Subsequent to shock-strut stroking

$$\ddot{z}_{w,b} = \frac{-F_{A,ss} - 0.5L_w + F_{wB} + m_w g \cos(\theta + \alpha)}{m_w} + \ddot{\alpha} d_{ew}$$

APPENDIX A

Wing-mass-center motion in gravity-axis system

$$\ddot{x}_{w,g} = \ddot{x}_{w,b} \cos(\theta + \alpha) + \ddot{z}_{w,b} \sin(\theta + \alpha)$$

$$\ddot{z}_{w,g} = \ddot{z}_{w,b} \cos(\theta + \alpha) - \ddot{x}_{w,b} \sin(\theta + \alpha)$$

Fuselage-mass-center motion in gravity-axis system

$$\ddot{x}_{f,g} = \ddot{x}_{c,g} - \ddot{\theta} d_{cf} \sin(\lambda_{cf} + \theta) - \dot{\theta}^2 d_{cf} \cos(\lambda_{cf} + \theta)$$

$$\ddot{z}_{f,g} = \ddot{z}_{c,g} - \ddot{\theta} d_{cf} \cos(\lambda_{cf} + \theta) + \dot{\theta}^2 d_{cf} \sin(\lambda_{cf} + \theta)$$

Wing-gear-interface motion in body-axis system

$$\ddot{x}_{wG,b} = \ddot{x}_{c,b} + \dot{\alpha}^2 (d_{ew} + d_{wwG}) + \ddot{\theta} d_{cwG} \sin(\lambda_{cwG} - \alpha) + \dot{\theta}^2 d_{cwG} \cos(\lambda_{cwG} - \alpha)$$

$$\ddot{z}_{wG,b} = \frac{-F_{A,ss} - 0.5L_w + F_{wB} + m_w g \cos(\theta + \alpha)}{m_w} + \dot{\alpha}(d_{ew} + d_{wwG})$$

Shock-strut motion in body-axis system

$$\ddot{s}_b = \ddot{z}_{wG,b} - \ddot{z}_{h,b} - \dot{\alpha}^2 l_{ss}$$

Motion of elastic axis at spanwise location of wing mass center:

Prior to shock-strut stroking

$$\ddot{z}_{ew,b} = \frac{F_{G,Z} \cos(\theta + \alpha) + F_{G,X} \sin(\theta + \alpha) + (m_w + m_h) g \cos(\theta + \alpha) - 0.5L_w + F_{wB}}{m_w + m_h}$$

Subsequent to shock-strut stroking

$$\ddot{z}_{ew,b} = \frac{-F_{A,ss} - 0.5L_w + F_{wB} + m_w g \cos(\theta + \alpha)}{m_w}$$

APPENDIX A

Motion of elastic axis at spanwise location of wing mass center relative to fuselage

$$\ddot{z}_{er,b} = \ddot{z}_{ew,b} - \ddot{z}_{c,b} + \ddot{\theta} x_{ce,b} + \dot{\theta}^{2} z_{ce,b}$$

Rotational motion of wing about elastic axis and relative to fuselage:

Prior to shock-strut stroking

$$\ddot{\alpha}_e = \frac{\left[\begin{array}{l} -M_{ef} + F_{G,X} l_{ss} \cos(\theta + \alpha) - F_{G,Z} l_{ss} \sin(\theta + \alpha) - m_h g l_{ss} \sin(\theta + \alpha) \\ + F_{G,Z}(d_{ew} + d_{wwG}) \cos(\theta + \alpha) + F_{G,X}(d_{ew} + d_{wwG}) \sin(\theta + \alpha) \\ + m_h g(d_{ew} + d_{wwG}) \cos(\theta + \alpha) + m_w g d_{ew} + M_a \end{array}\right]}{I_e + m_w d_{ew}^2 + I_a + m_h d_{eh}^2}$$

Subsequent to shock-strut stroking

$$\ddot{\alpha}_e = \frac{\left[\begin{array}{l} -M_{ef} - F_{A,ss}(d_{ew} + d_{wwG}) + m_w g d_{ew} \cos(\theta + \alpha) + F_{G,X} l_{ss} \cos(\theta + \alpha) \\ - F_{G,Z} l_{ss} \sin(\theta + \alpha) - m_h g l_{ss} \sin(\theta + \alpha) + M_a \end{array}\right]}{I_e + m_w d_{ew}^2 + I_a + m_h d_{eh}^2}$$

Wheel angular acceleration about hub

$$\ddot{\phi} = \frac{M_a + M_{br}}{I_a}$$

Brake-control-sensor acceleration about hub

$$\ddot{\beta} = 2\omega_{n,\beta} \frac{C_\beta}{C_{\beta,cr}}(\dot{\phi} - \dot{\beta}) + \omega_{n,\beta}^2(\phi - \beta)$$

Pitch angular acceleration about airplane center of gravity

$$\ddot{\theta} = \frac{\left[\begin{array}{l} -0.5L_t d_3 + 0.5D_f d_4 + 0.5D_t d_4 + 0.5L_w d_5 \cos\alpha - 0.5L_w d_6 \sin\alpha \\ -0.5D_w d_{cw,x} \cos\alpha \sin\alpha - F_{A,ss} d_1 + F_{G,X} d_2 \cos(\theta + \alpha) \\ -F_{G,Z} d_2 \sin(\theta + \alpha) + M_n \end{array}\right]}{I_{YY}}$$

APPENDIX B

DESCRIPTION OF LANDING GEAR

The landing gear simulated in this paper was originally designed for a small airplane having a gross mass of approximately 2268 kg (5000 lbm). (See ref. 7.) The gear is a cantilevered type with a conventional oleo-pneumatic shock strut. The tire is a 0.69-m (27-in.) diameter type I (smooth contour) which was inflated to 221 kPa (32 psi). The mass of the landing gear is 68 kg (150 lbm) and the unsprung mass is 59 kg (131 lbm).

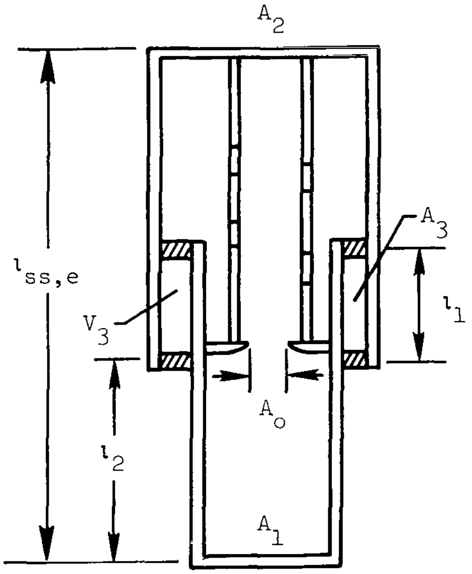

Sketch (d)

The important geometric characteristics of the landing-gear shock strut are illustrated in sketch (d), and the program input parameters are as follows:

Shock strut:

Pneumatic area, A_2	$0.00535\ m^2$	$(0.05762\ ft^2)$
Hydraulic area, A_1	$0.00437\ m^2$	$(0.04708\ ft^2)$
Primary orifice area, A_o	$0.00005\ m^2$	$(0.00056\ ft^2)$
Pressurized pneumatic volume, V_2	$0.0010\ m^3$	$(0.03545\ ft^3)$
Charging pressure, $p_{o,a}$	299.9 kPa	(6264 psfa)
Bearing separation for fully extended shock strut, l_1	0.16828 m	(0.5521 ft)
Axial length from hub to lower bearing for fully extended shock strut, l_2	0.6785 m	(2.22604 ft)
Mass of airplane acting on each main gear, W_1	1094 kg	(2411 lbm)
Unsprung gear mass, W_2	59 kg	(131 lbm)

Fully extended length of shock strut, $l_{ss,e}$	0.9674 m (3.174 ft)
Friction coefficient (upper bearing), $\mu_{ss,u}$	0.15
Friction coefficient (lower bearing), $\mu_{ss,l}$	0.15
Volume between piston and cylinder, V_3	0 m^3 (0 ft^3)
Area between piston and cylinder, A_3	0 m^2 (0 ft^2)
Specific weight of hydraulic fluid, γ_H	8226 N/m^3 (52.36 lbf/ft^3)
Dynamic viscosity of hydraulic fluid, μ_H	0.00862 N-sec/m^2 (0.00018 lbf-sec/ft^2)
Mass density of hydraulic fluid, ρ_H	838 kg/m^3 (1.626 slugs/ft^3)
Volume of hydraulic fluid in fully extended strut, V_H	≈0.0014 m^3 (≈0.05 ft^3)

Wheel and tire:

Wheel flange diameter, d_f	0.39053 m (1.28125 ft)
Width of wheel rim, w_w	0.227 m (0.745 ft)
Unloaded diameter of tire, d	0.686 m (nominal 2.25 ft)
Maximum width of undeflected tire, w	0.245 m (0.805 ft)
Unloaded rated inflation tire pressure, p_r	482.63 kPa (10 080 psf)
Unloaded tire inflation pressure, p_o	220.6 kPa (4608 psf)
Pressure-rise parameter, κ	0.66
Vertical-force coefficient, C_Z	0.02

REFERENCES

1. Wignot, Jack E.; Durup, Paul C.; and Gamon, Max A.: Design Formulation and Analysis of an Active Landing Gear. Volume I. Analysis. AFFDL-TR-71-80, Vol. I, U.S. Air Force, Aug. 1971. (Available from DDC as AD 887 127L.)
2. Bender, E. K.; Berkman, E. F.; and Bieber, M.: A Feasibility Study of Active Landing Gear. AFFDL-TR-70-126, U.S. Air Force, July 1971. (Available from DDC as AD 887 451L.)
3. Smiley, Robert F.; and Horne, Walter B.: Mechanical Properties of Pneumatic Tires With Special Reference to Modern Aircraft Tires. NASA TR R-64, 1960. (Supersedes NACA TN 4110.)
4. Tung, C. C.; Penzien, J.; and Horonjeff, R.: The Effect of Runway Unevenness on the Dynamic Response of Supersonic Transports. NASA CR-119, 1964.
5. Batterson, Sidney A.: A Study of the Dynamics of Airplane Braking Systems as Affected by Tire Elasticity and Brake Response. NASA TN D-3081, 1965.
6. Milwitzsky, Benjamin; Lindquist, Dean C.; and Potter, Dexter M.: An Experimental Study of Applied Ground Loads in Landing. NACA Rep. 1248, 1955. (Supersedes NACA TN 3246.
7. Milwitzsky, Benjamin; and Cook, Francis E.: Analysis of Landing-Gear Behavior. NACA Rep. 1154, 1953. (Supersedes NACA TN 2755.)
8. Diehl, Walter Stuart: Engineering Aerodynamics. Sixth ed. Ronald Press Co., c.1936.
9. Lynch, Urban H. D.: Takeoff and Landing Analysis (TOLA) Computer Program. Part 1: Capabilities of the Takeoff and Landing Analysis Computer Program. AFFDL-TR-71-155, Pt. 1, U.S. Air Force, Feb. 1972. (Available form DDC as AD 741 942.)

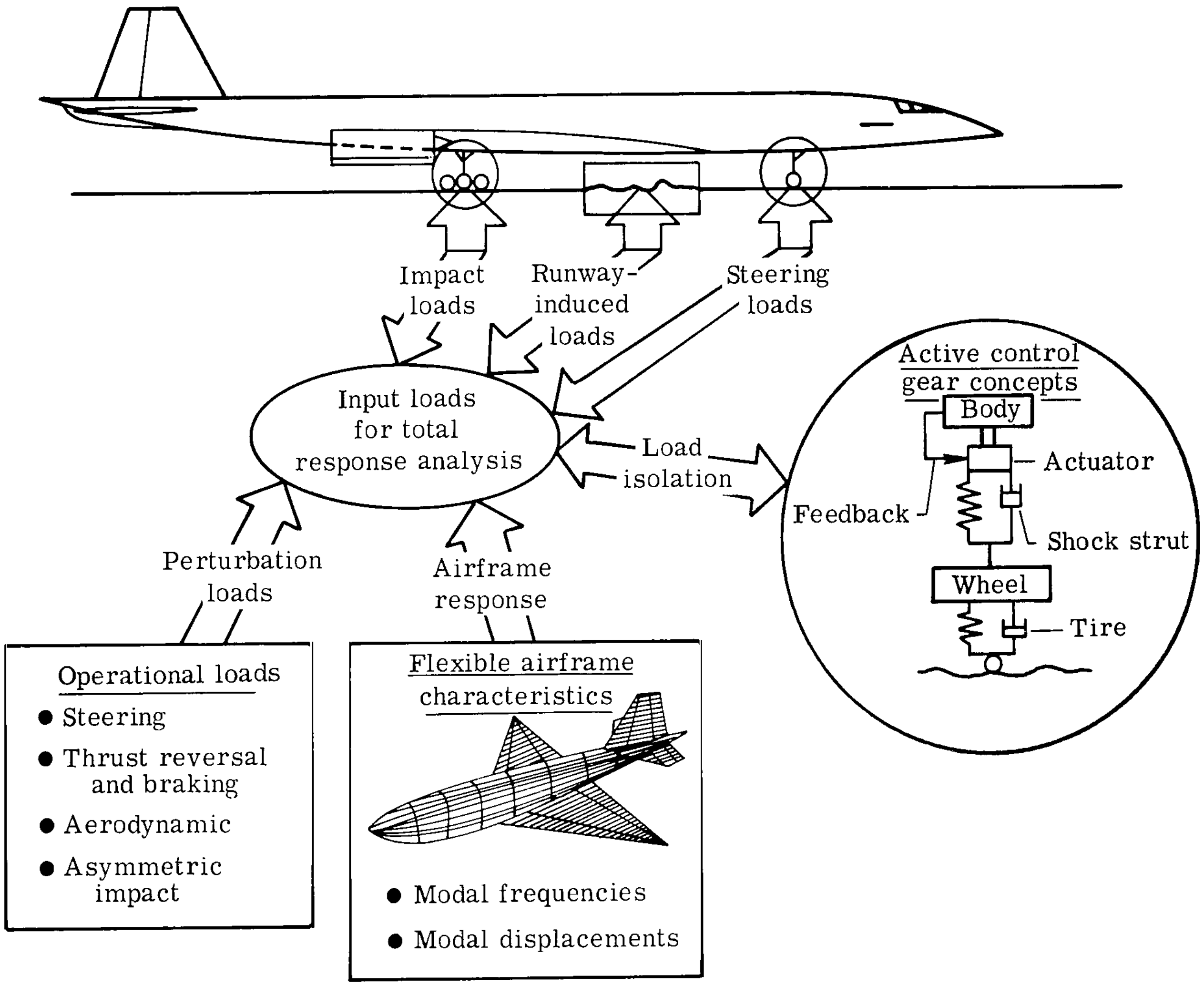

Figure 1.- Variables considered significant for analyzing active control landing gear systems.

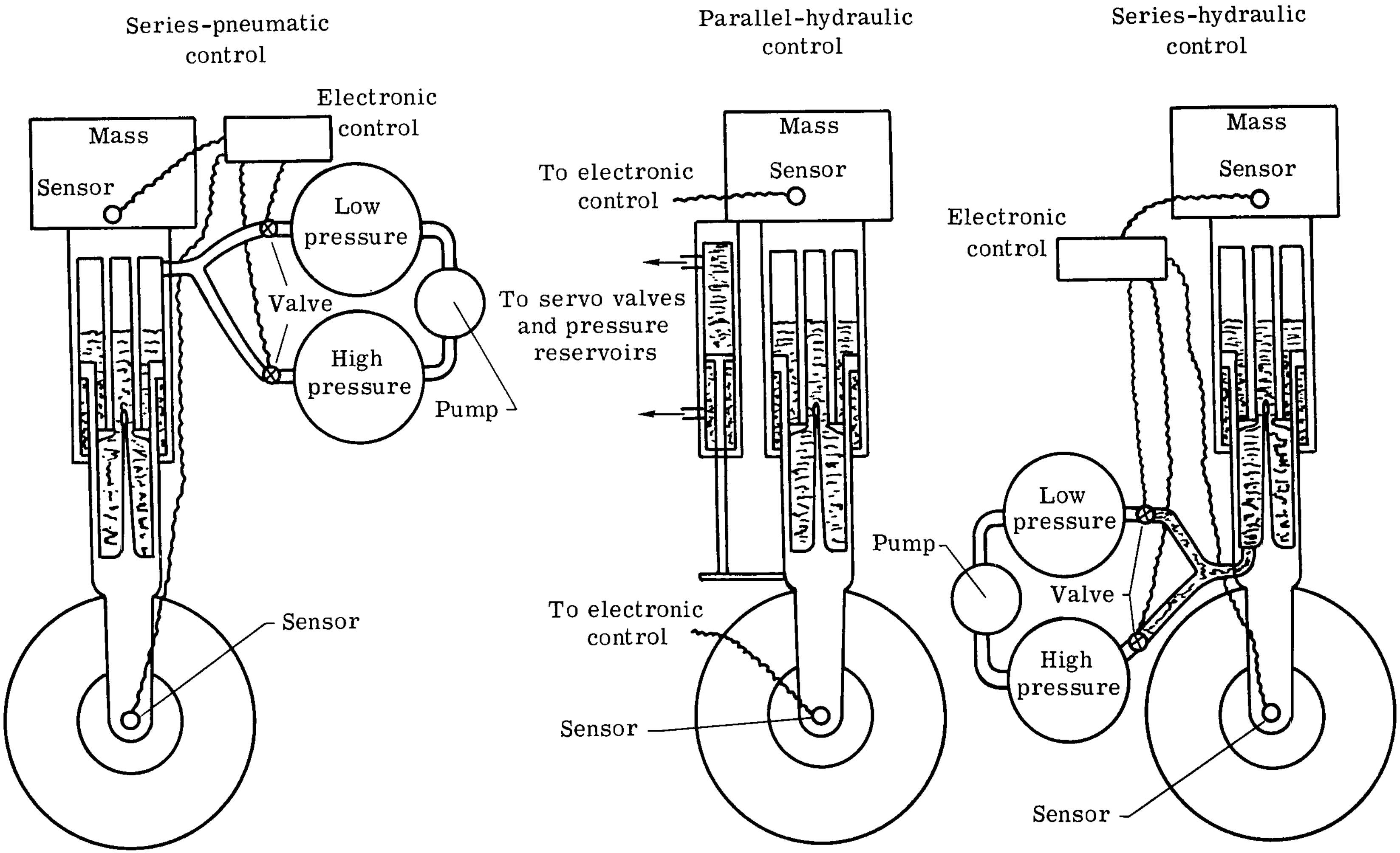

Figure 2.- Active control concepts for airplane landing gears.

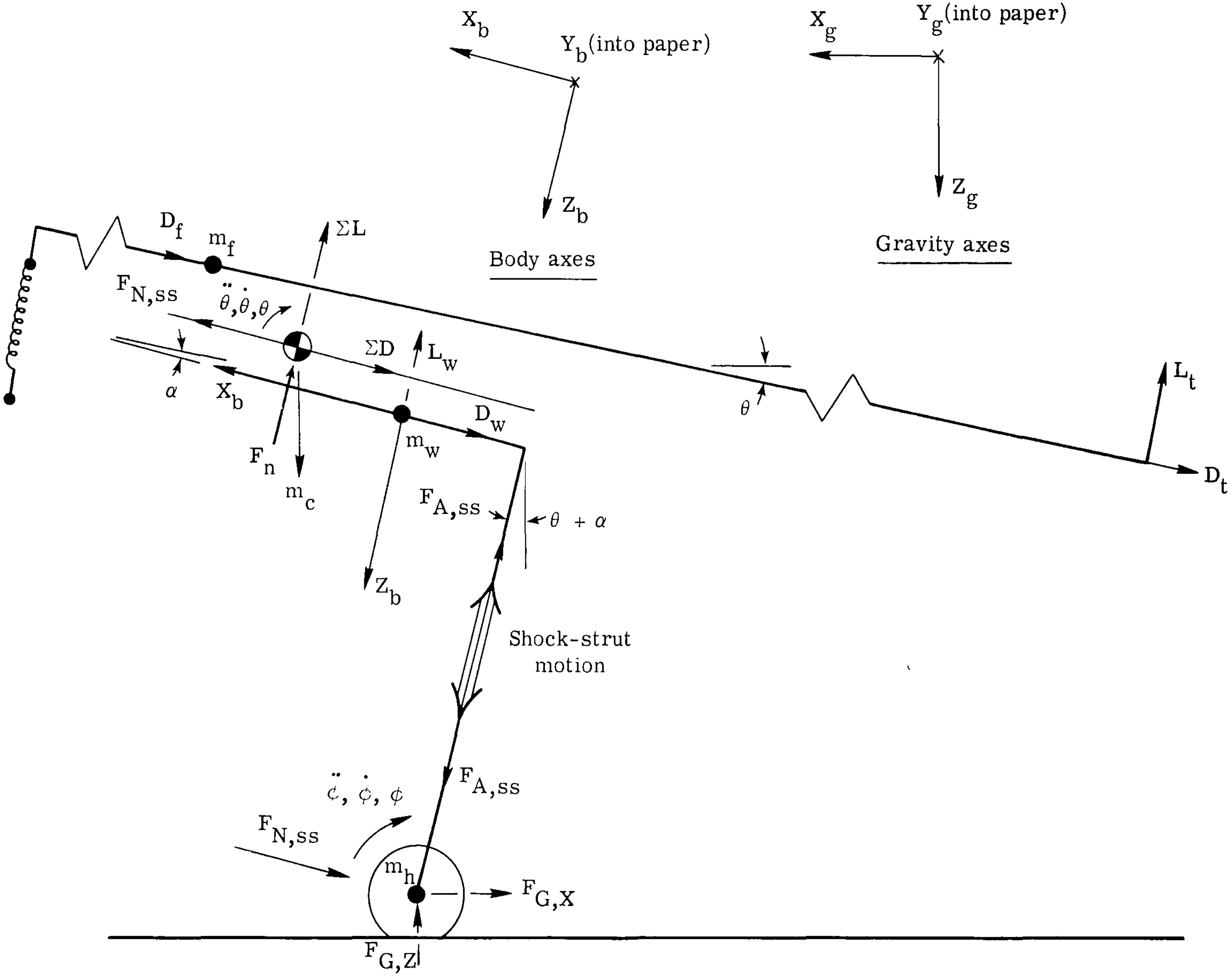

Figure 3.- Definition of axes and forces for rigid-airframe option.

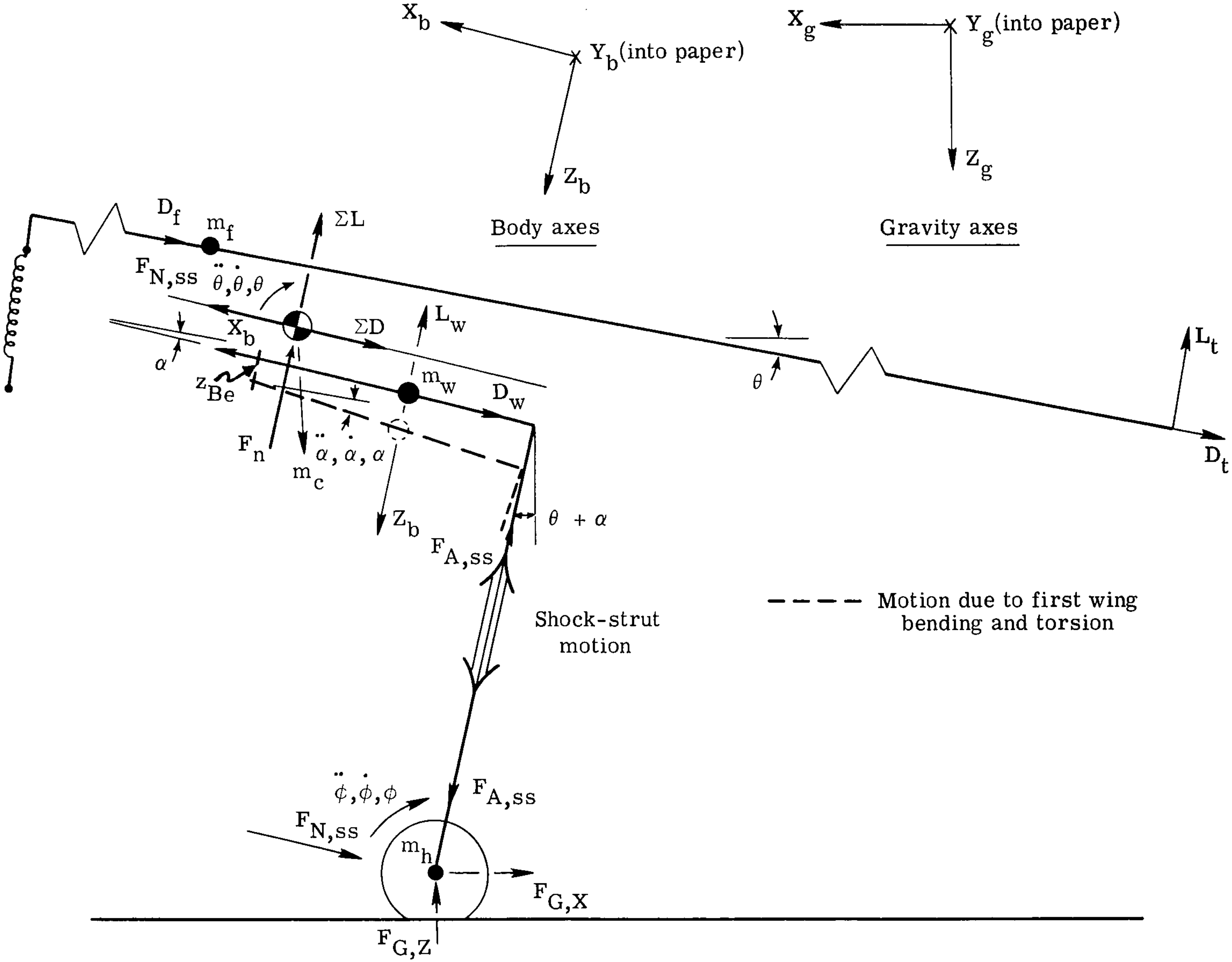

Figure 4.- Definition of axes and forces for rigid-fuselage—elastic-wing option.

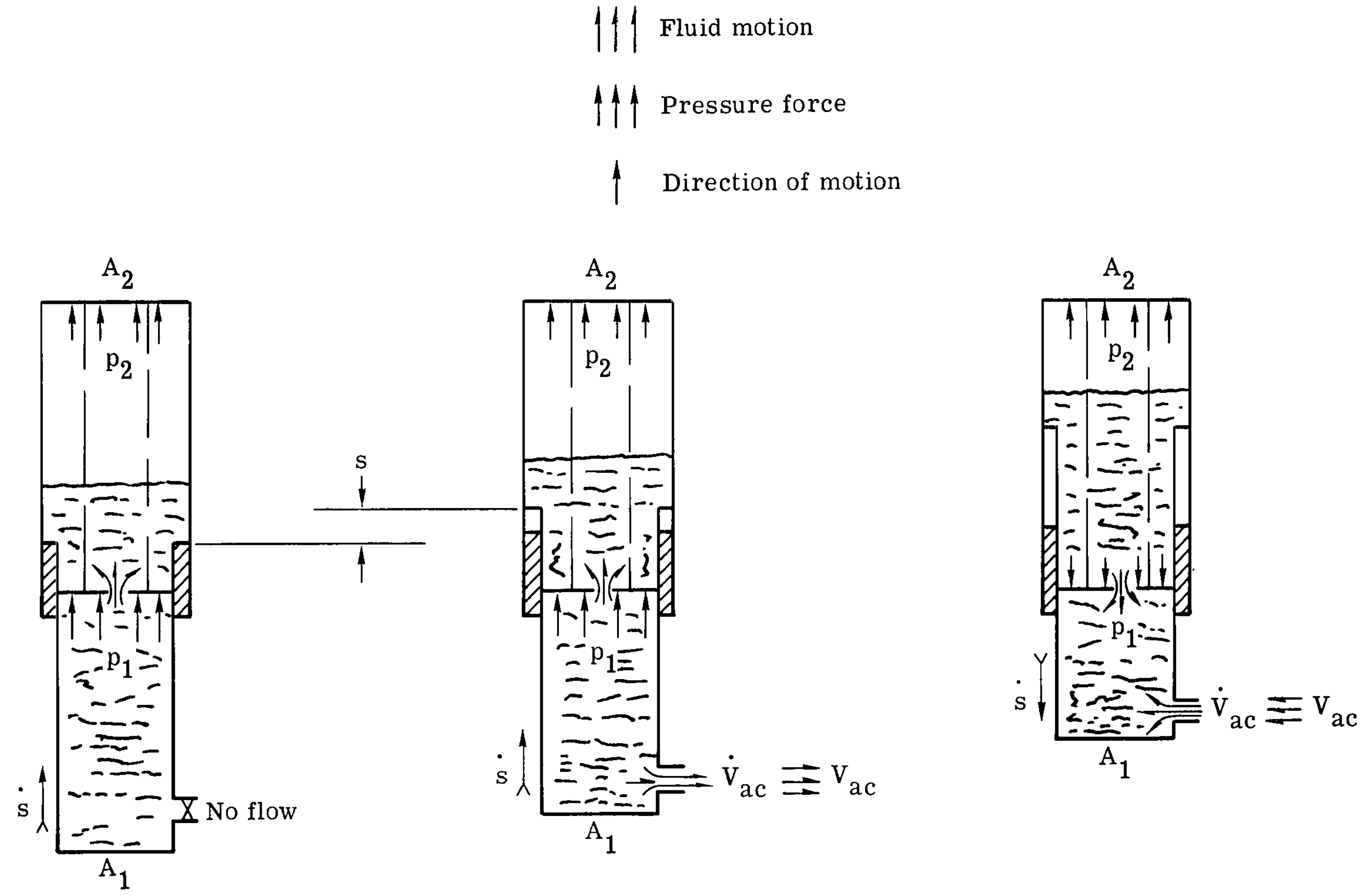

(a) Passive gear phase. Compressing with wing force less than limit force.

(b) Active gear phase. Low-pressure operation; compressing; wing force greater than limit force.

(c) Active gear phase. High-pressure operation; extending; wing force less than limit force.

Figure 5.- Operational phases of series-hydraulic active control gear.

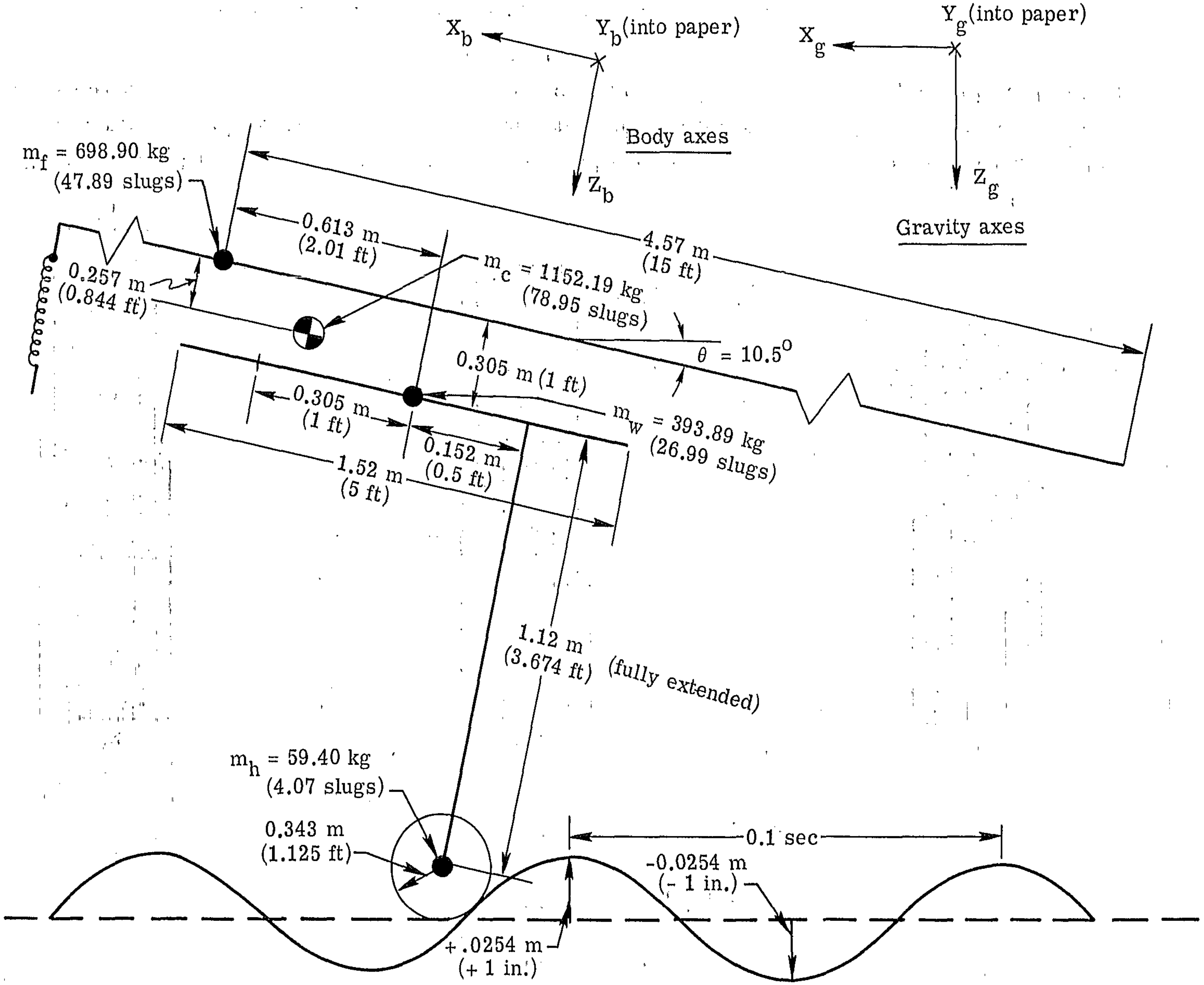

Figure 6.- Rigid-airframe configuration used for study. (Dimensions are not to scale.)

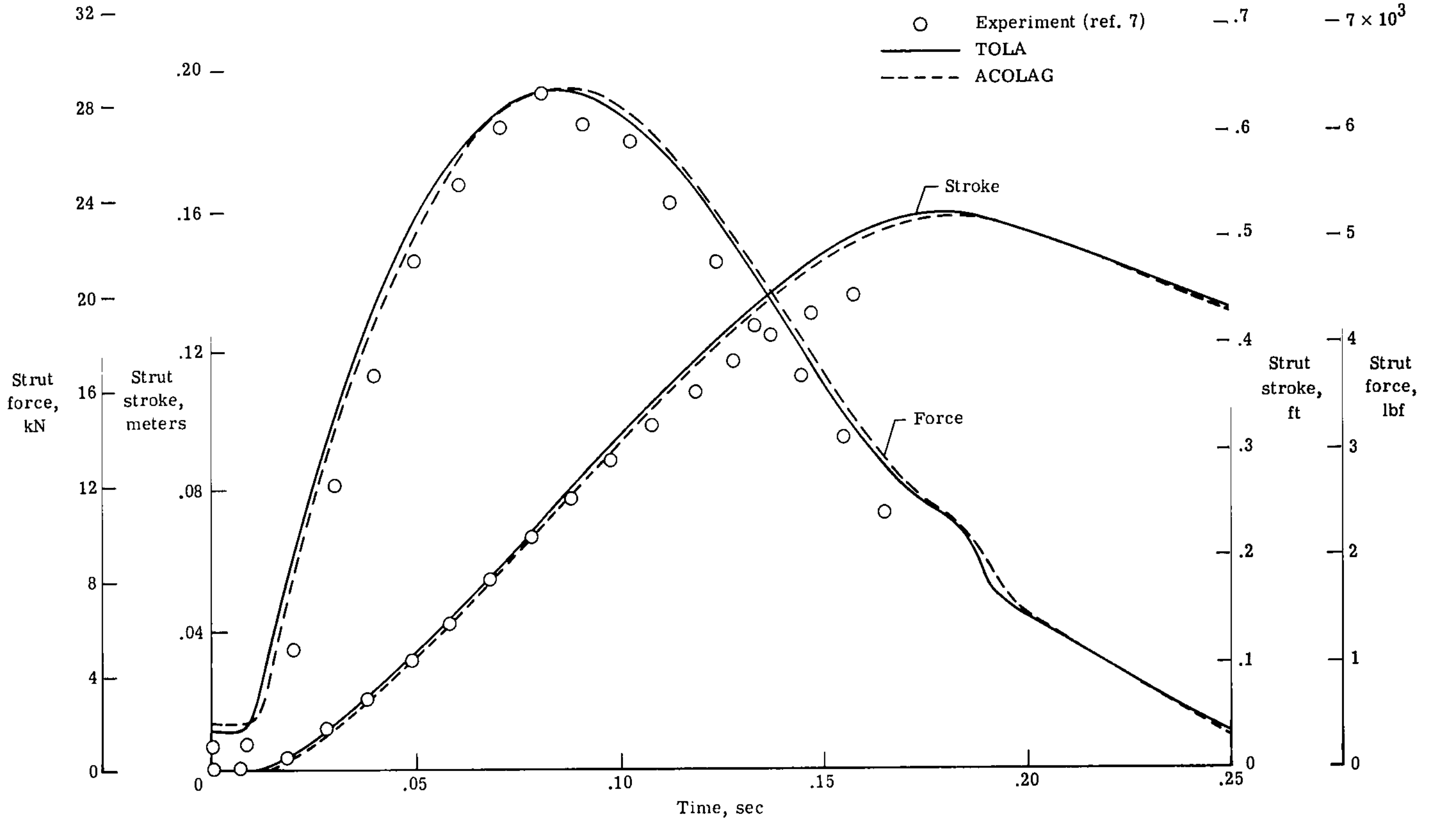

(a) Time histories of shock-strut force and stroke.

Figure 7.- Comparison of computed results obtained from ACOLAG and TOLA with experimental data for a vertical drop onto a flat stationary surface. $\theta = 0^{\circ}$; $\dot{z}_{c,g} = 2.7$ m/sec (8.8 ft/sec); $\dot{x}_{c,g} = 0$ m/sec (0 ft/sec).

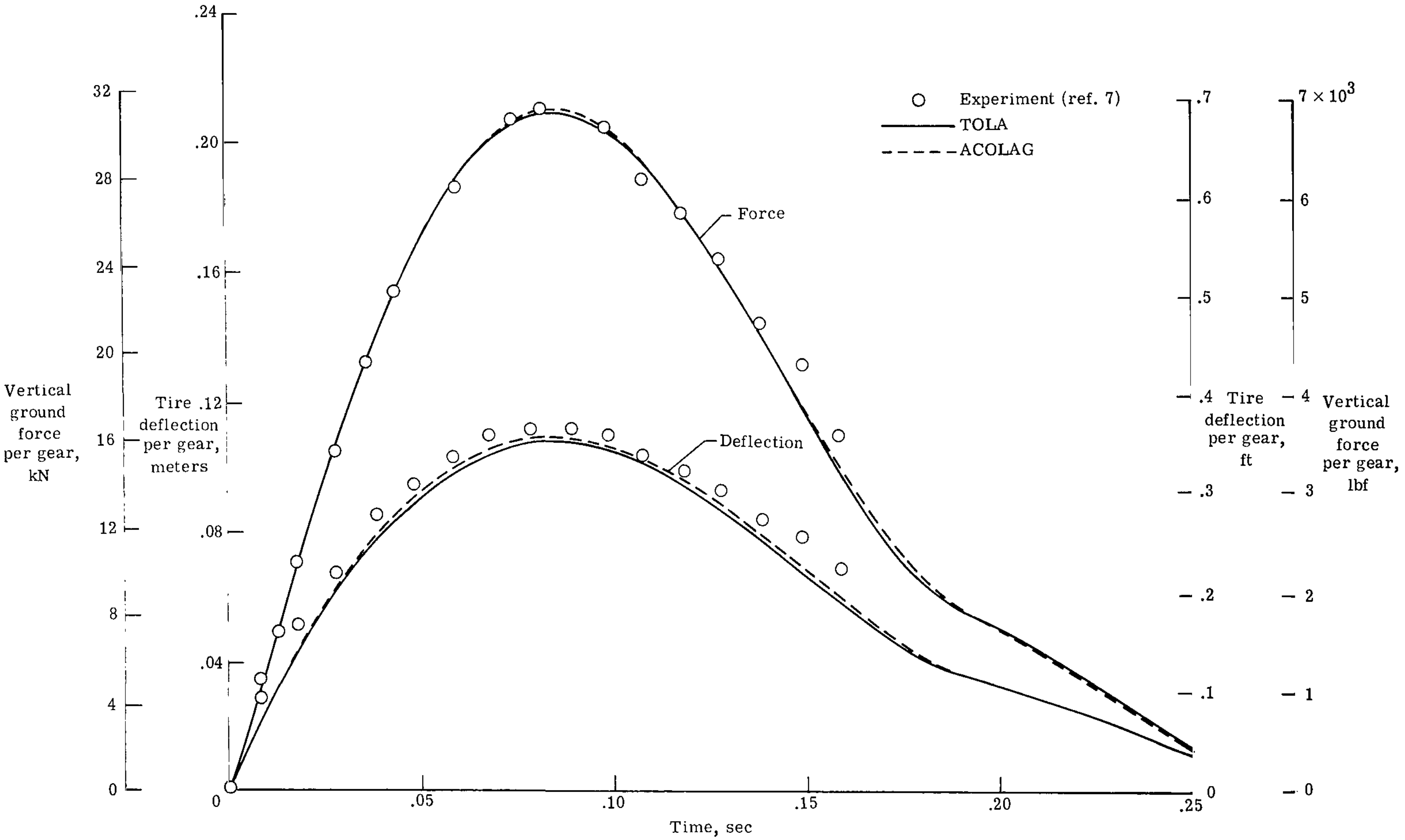

(b) Time histories of vertical ground force and tire deflection.

Figure 7.- Continued.

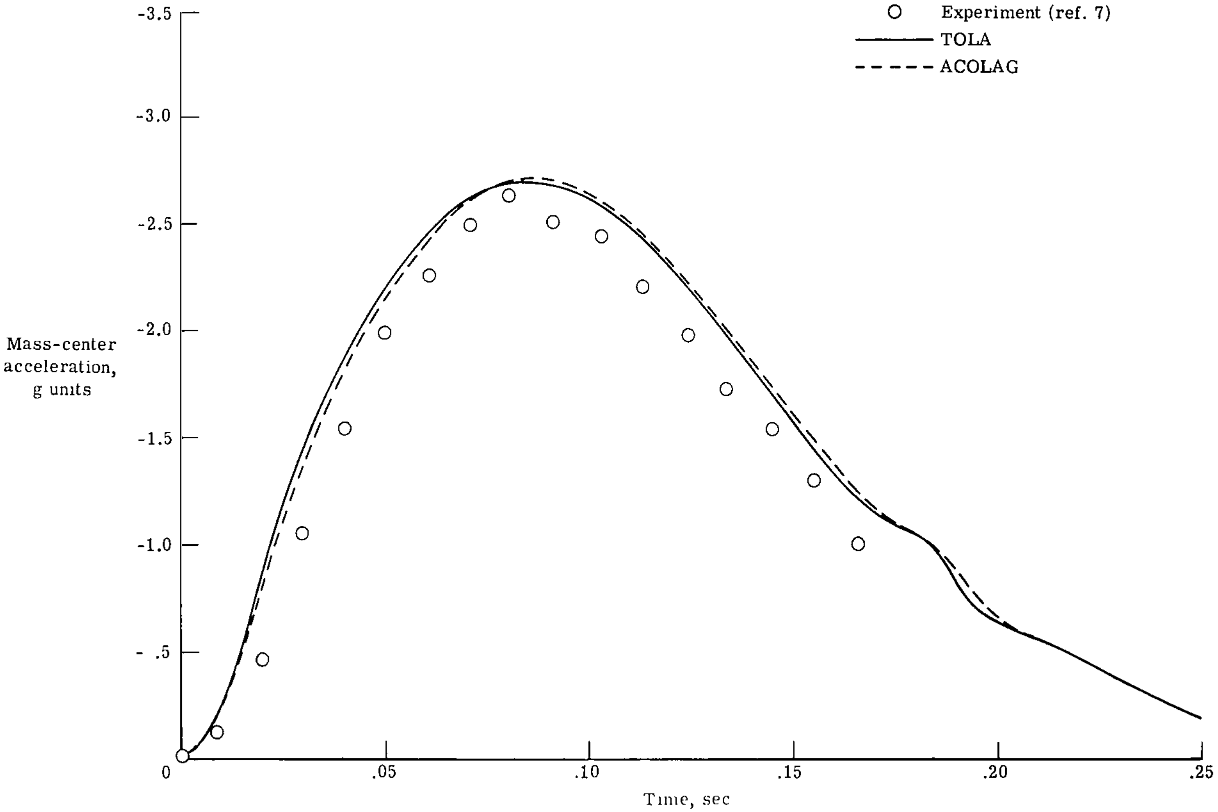

(c) Time histories of mass-center acceleration.

Figure 7.- Concluded.

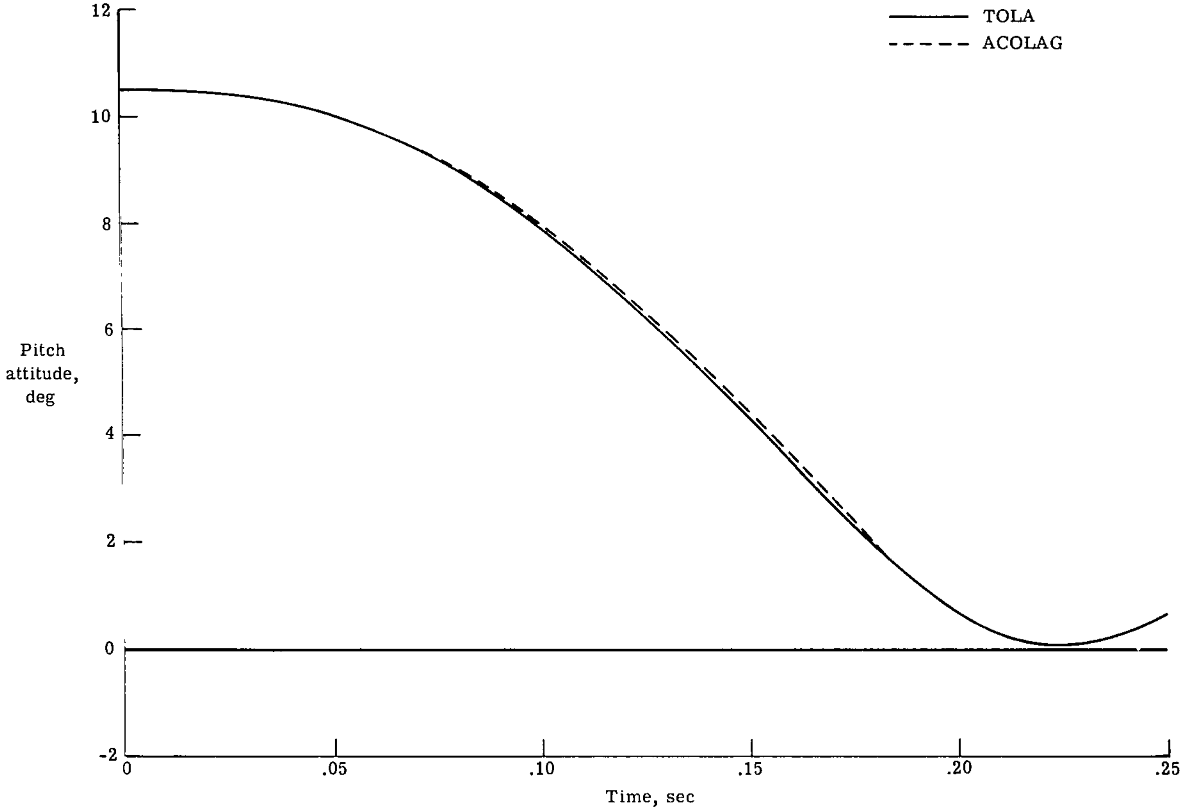

(a) Time histories of pitch attitude.

Figure 8.- Comparison of computed results from ACOLAG and TOLA for landing-impact simulation. $\theta = 10.5^{\circ}$; $\dot{z}_{c,g} = 2.7$ m/sec (8.8 ft/sec); $\dot{x}_{c,g} = 45.7$ m/sec (150 ft/sec).

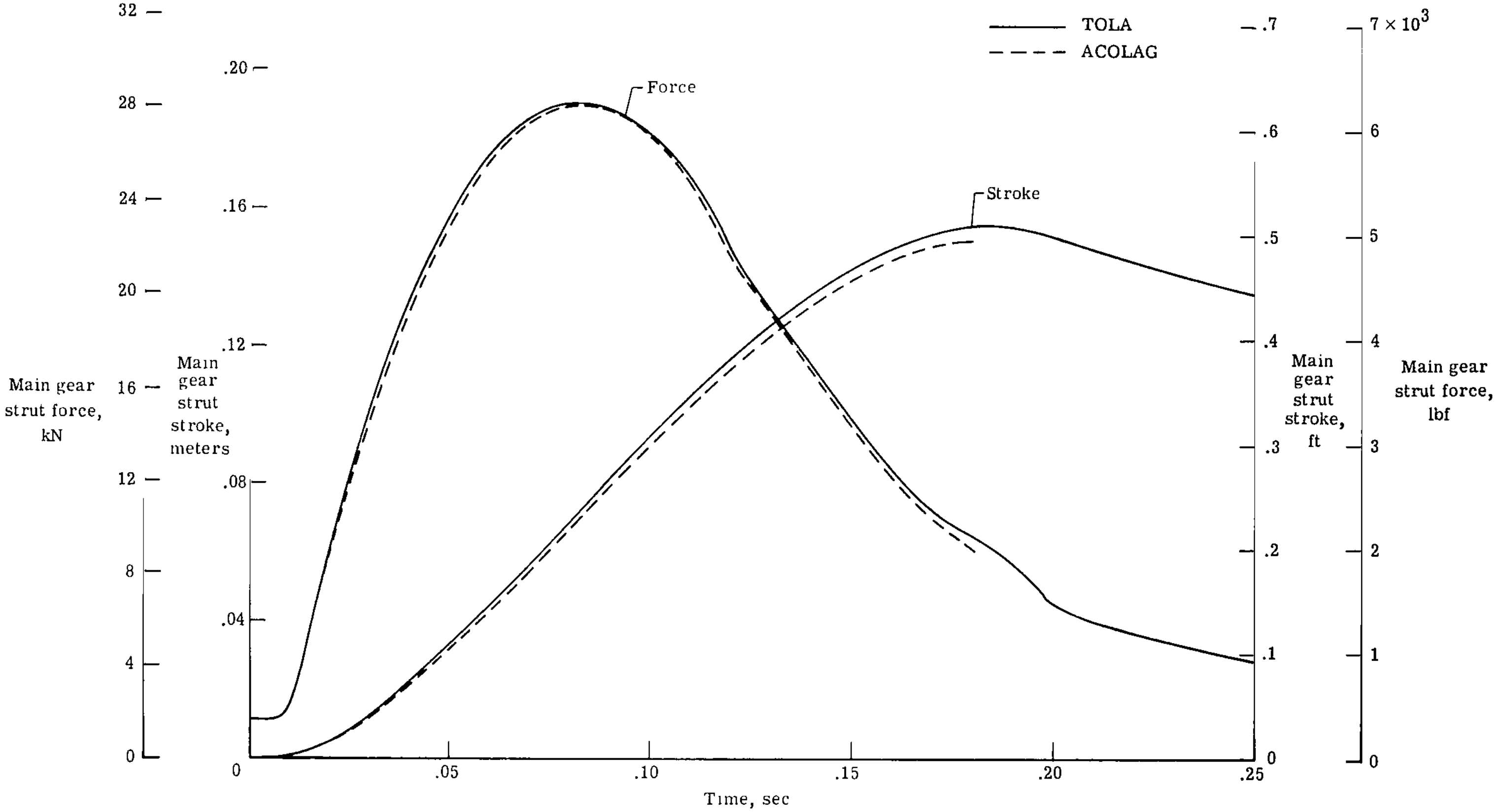

(b) Time histories of shock-strut force and stroke.

Figure 8. - Continued.

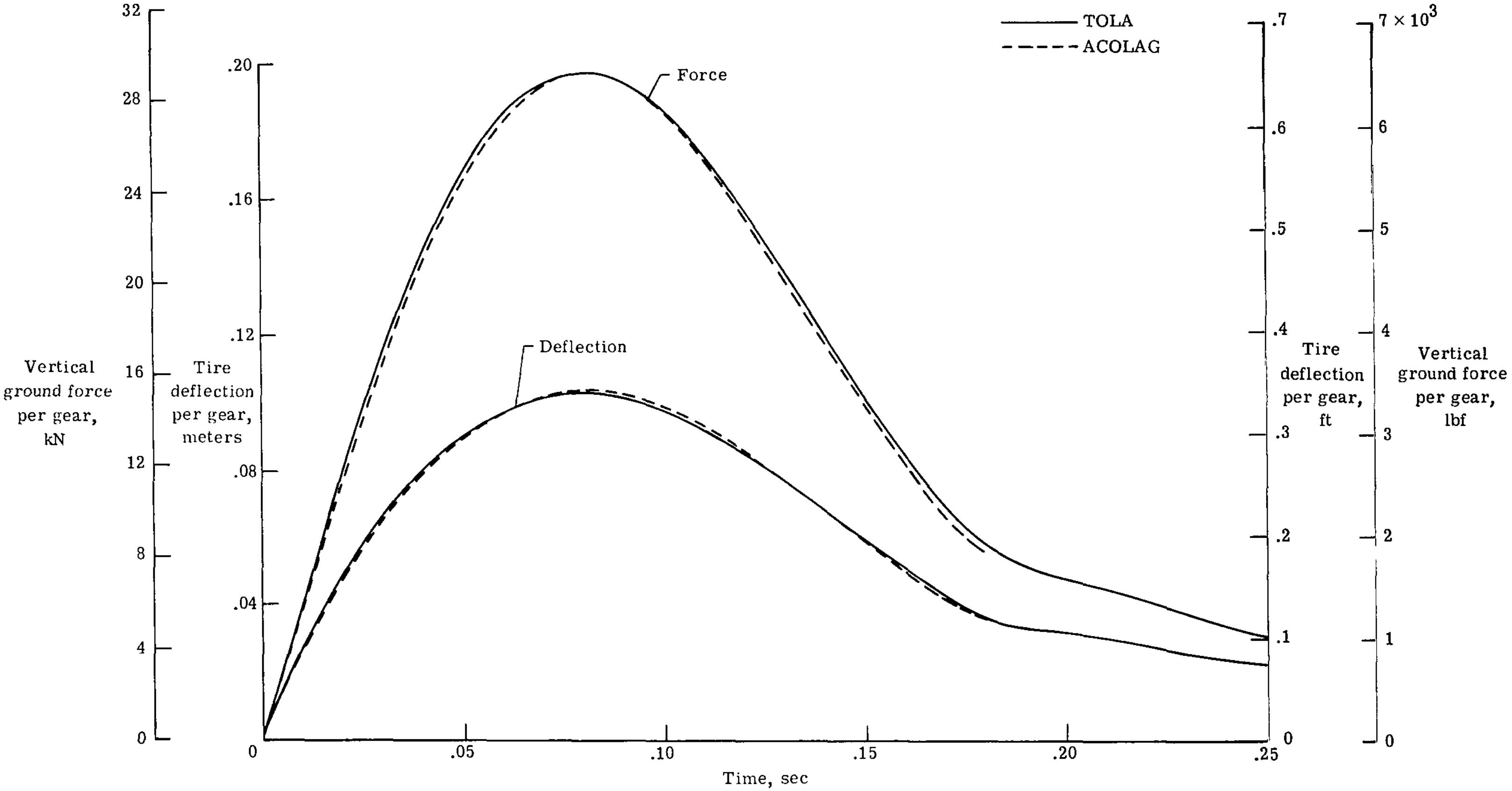

(c) Time histories of vertical ground force and tire deflection.

Figure 8.- Continued.

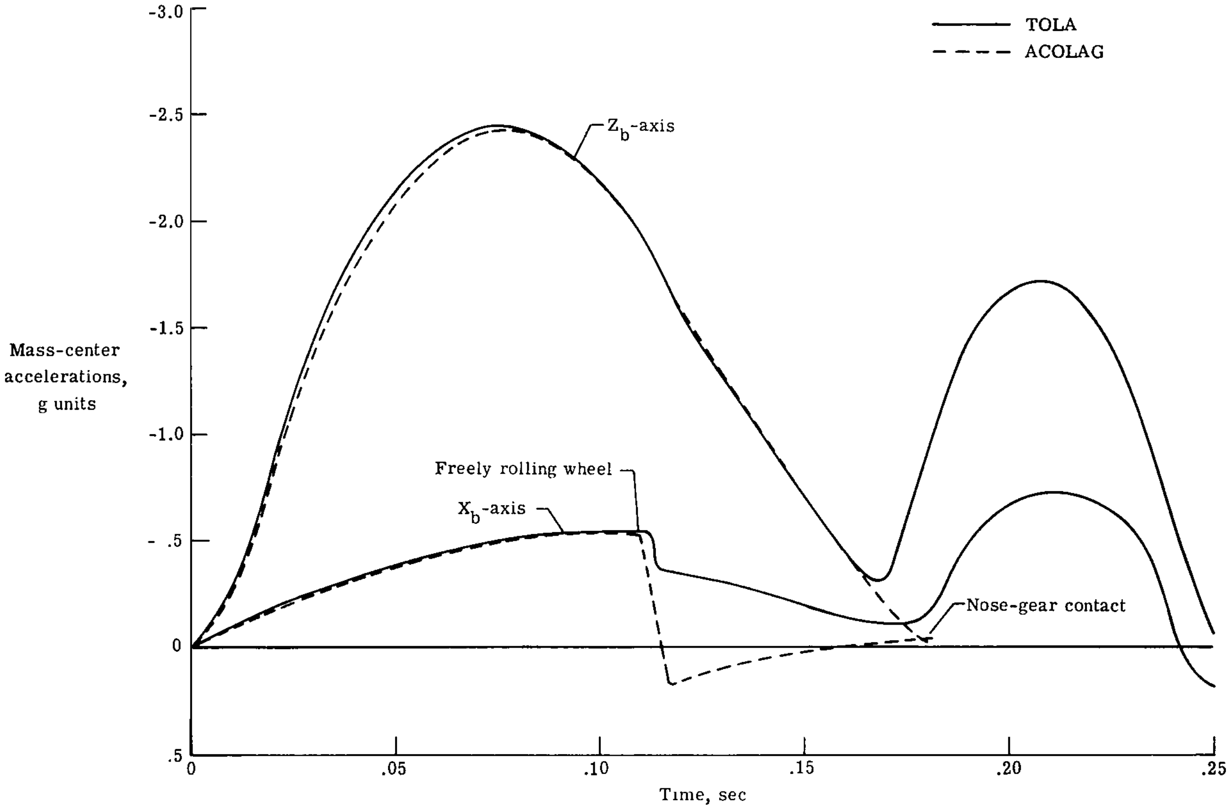

(d) Time histories of mass-center acceleration.

Figure 8.- Concluded.

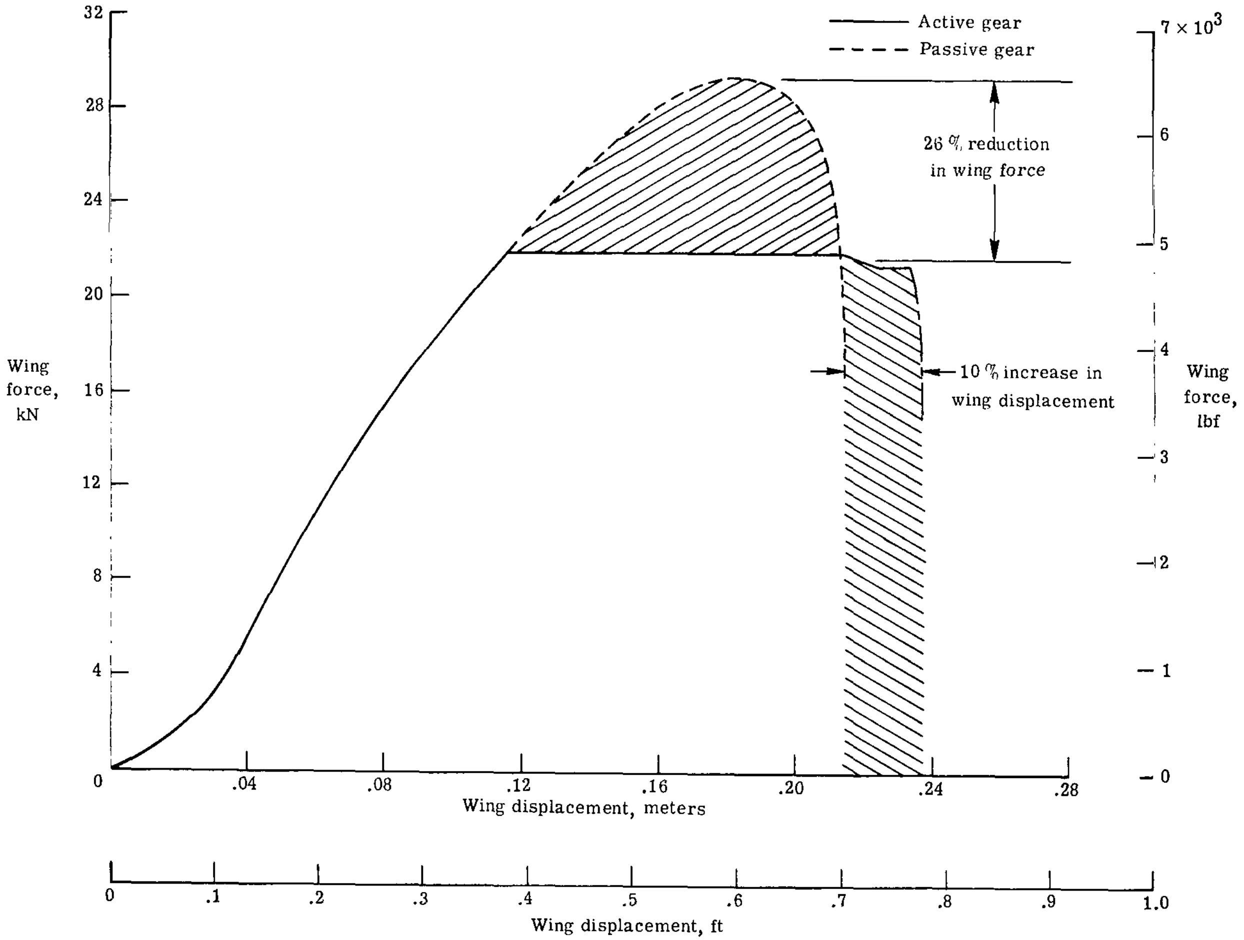

(a) Wing force as a function of wing displacement.

Figure 9.- Comparison of computed results for modified passive and active gears for a vertical drop onto a flat stationary surface. $\theta = 0^{\circ}$; $\dot{z}_{c,g} = 2.7$ m/sec (8.8 ft/sec); $\dot{x}_{c,g} = 0$ m/sec (0 ft/sec).

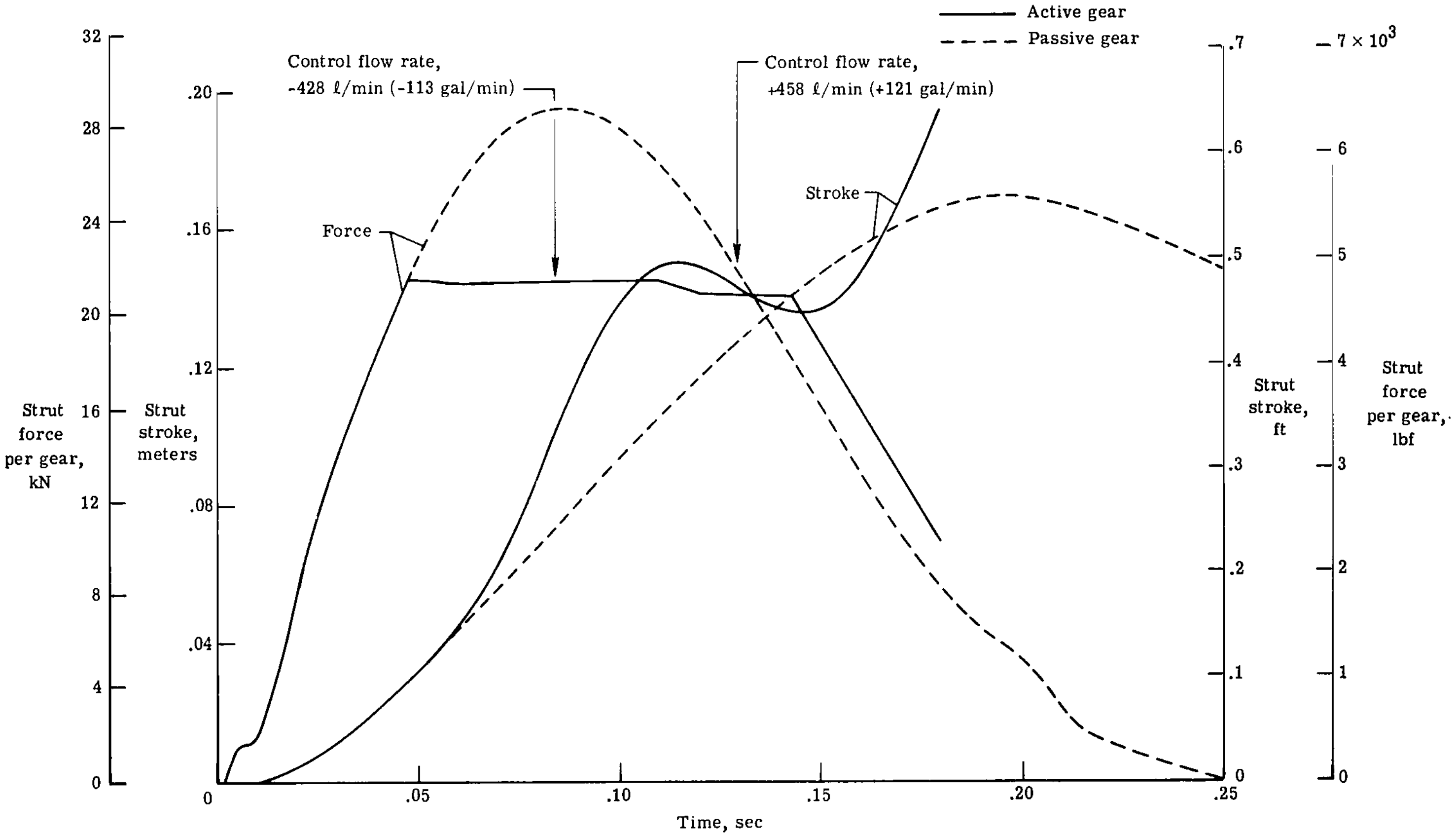

(b) Time histories of shock-strut force and stroke.

Figure 9.- Continued.

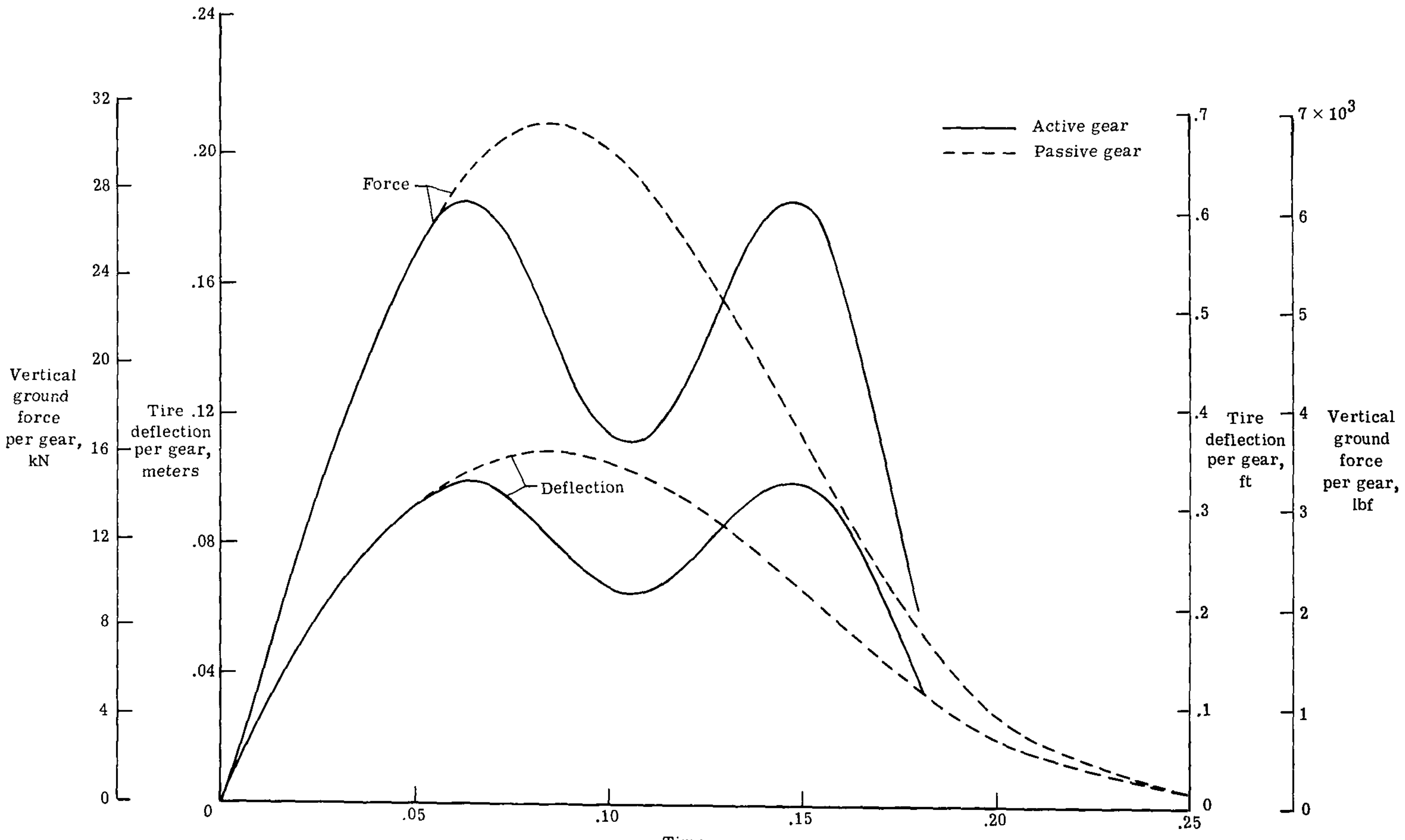

(c) Time histories of vertical ground force and tire deflection.

Figure 9. - Concluded.

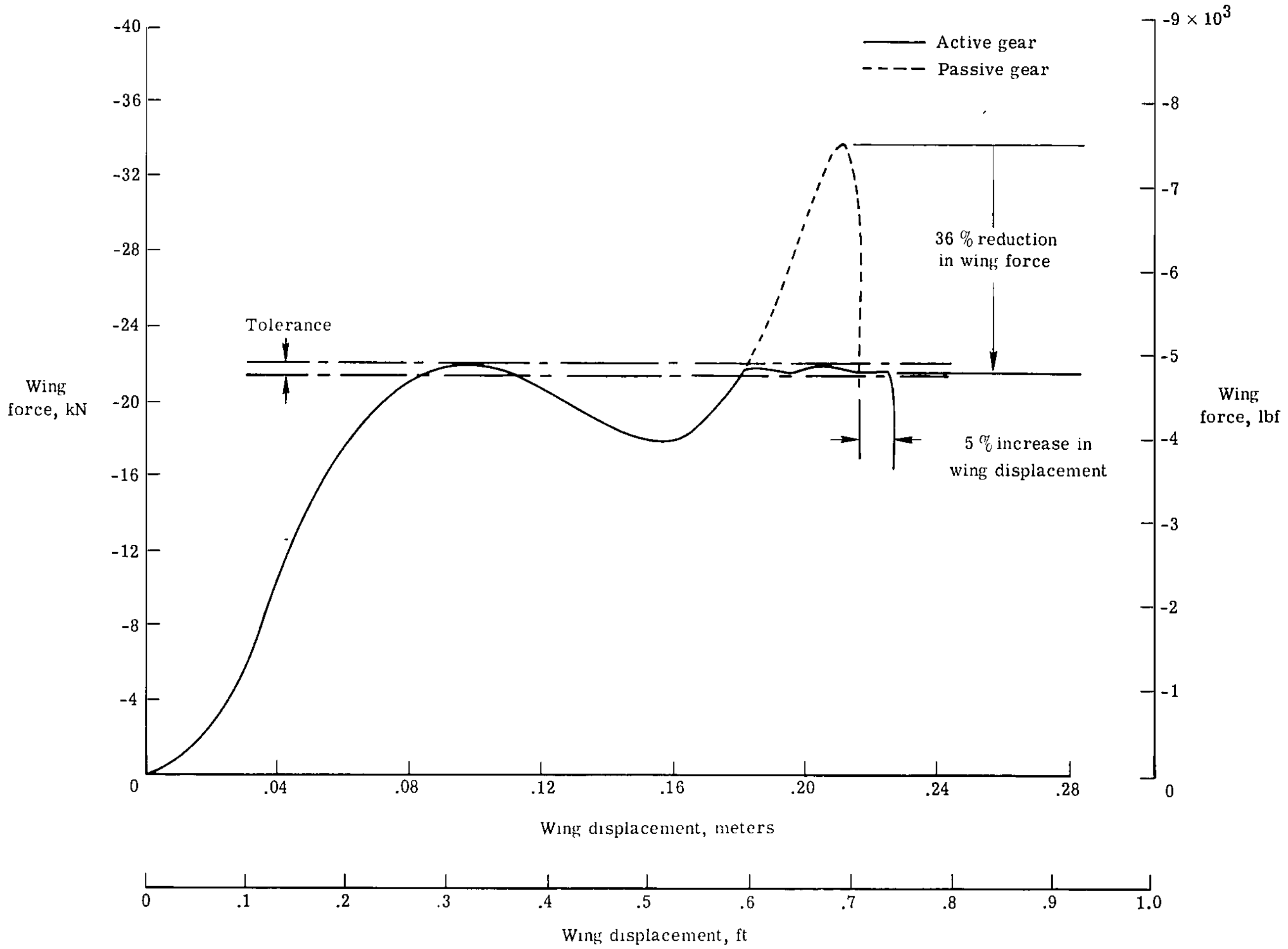

(a) Wing force as a function of wing displacement.

Figure 10.- Comparison of computed results for modified passive and active gears for a vertical drop onto a vertically oscillating surface. $\theta = 0^{\circ}$; $\dot{z}_{c,g} = 2.7$ m/sec (8.8 ft/sec); $\dot{x}_{c,g} = 0$ m/sec (0 ft/sec).

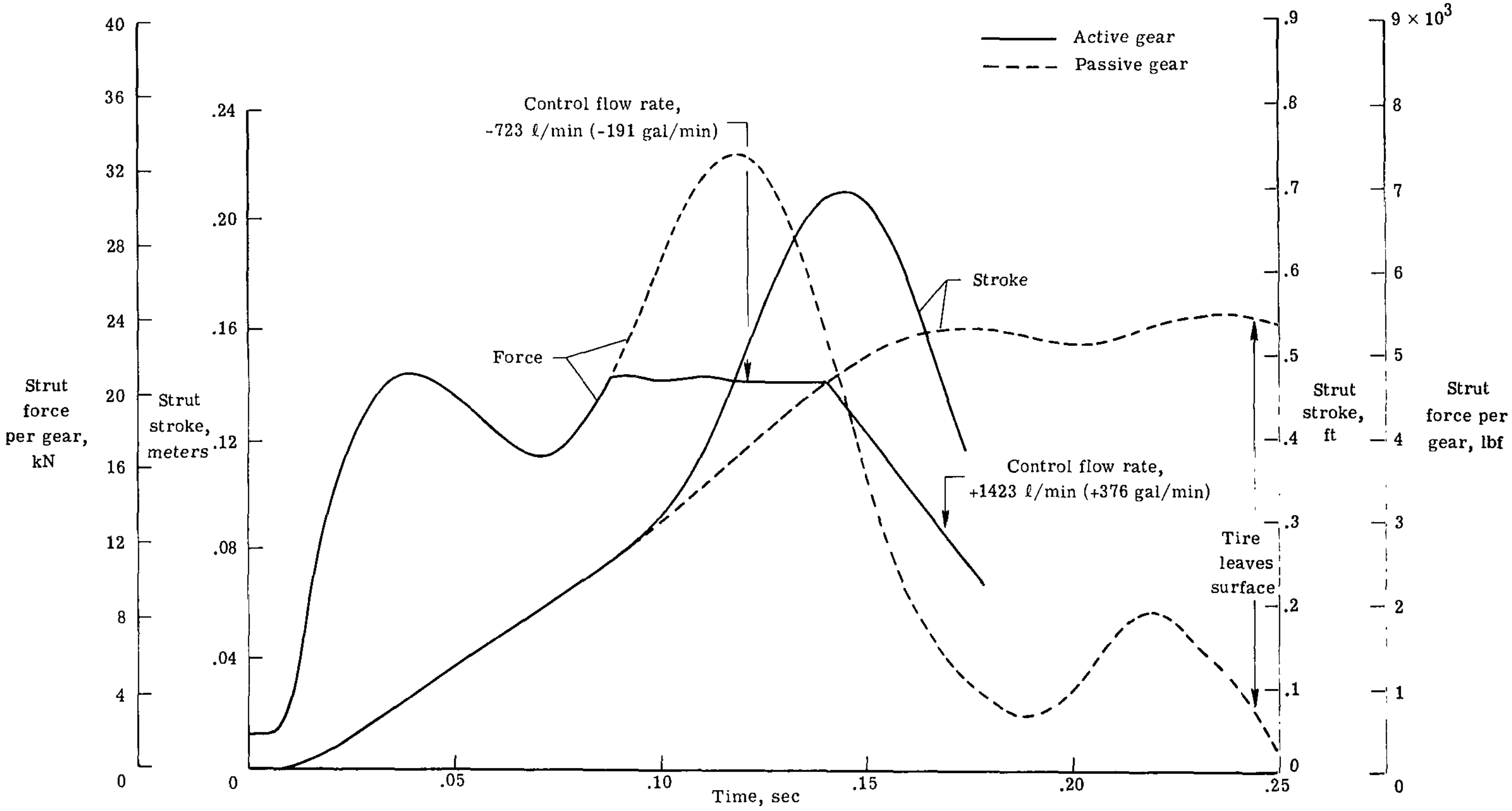

(b) Time histories of shock-strut force and stroke.

Figure 10. - Continued.

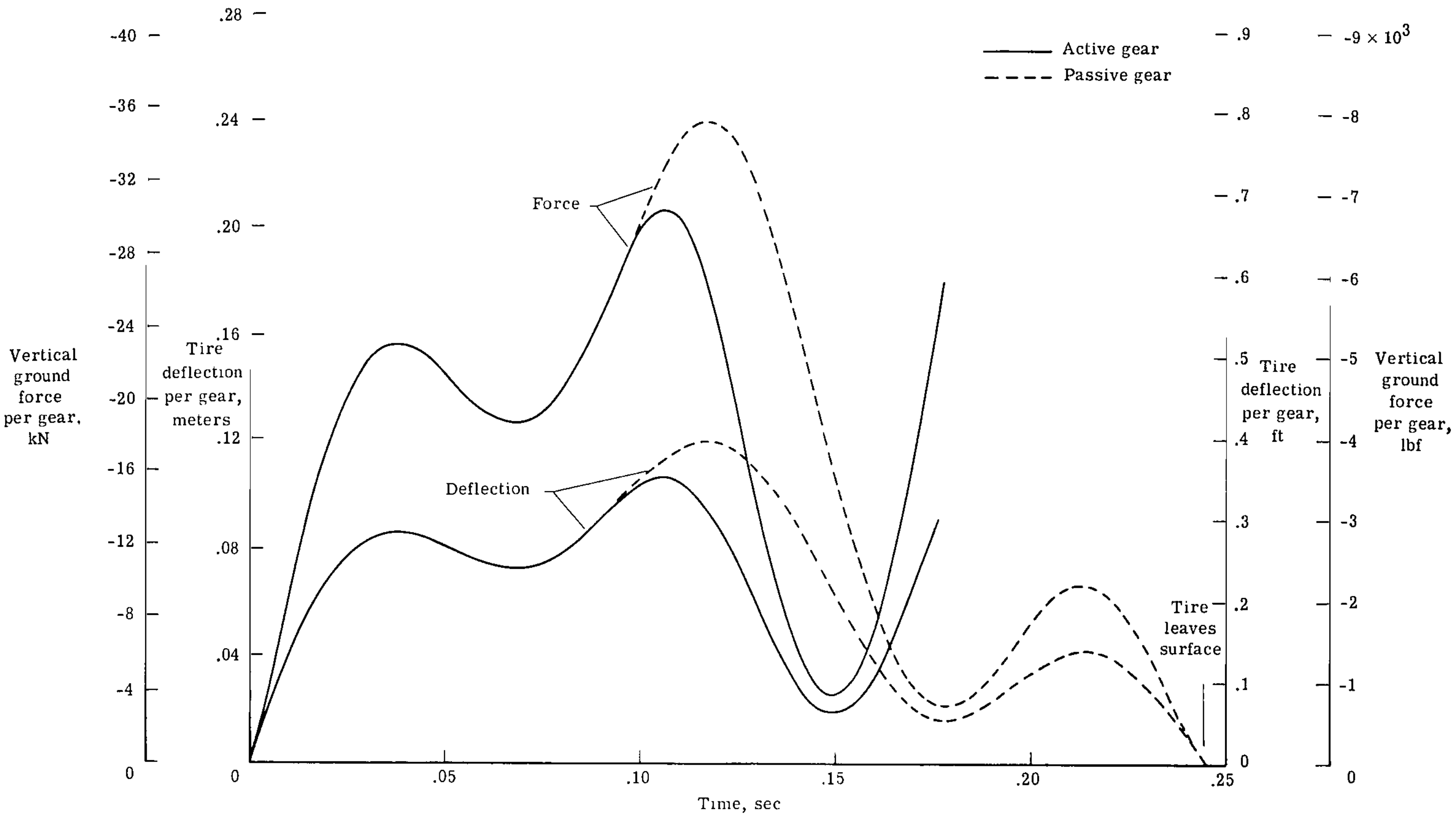

(c) Time histories of vertical ground force and tire deflection.

Figure 10.- Concluded.

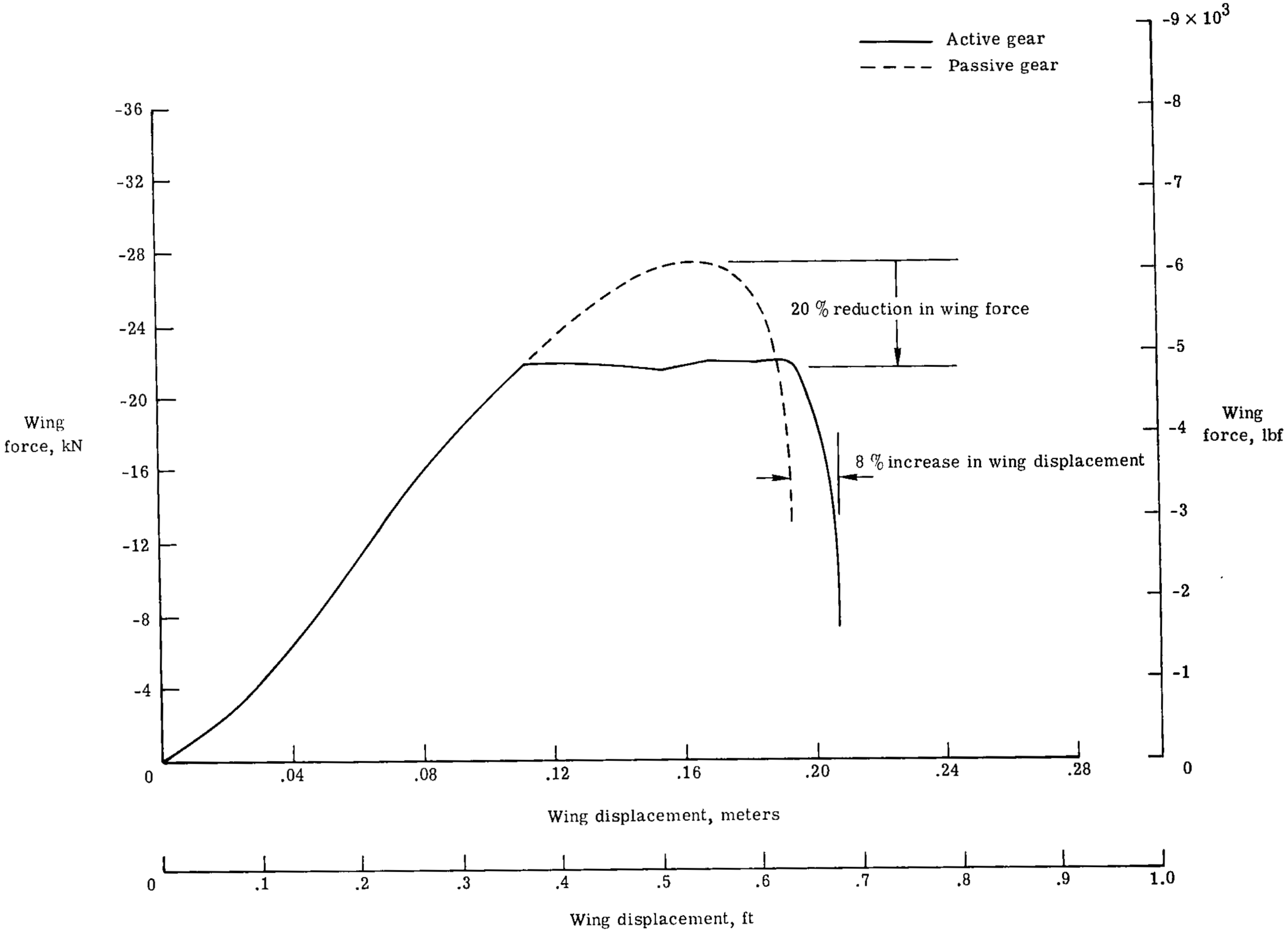

(a) Wing force as a function of wing displacement.

Figure 11. - Comparison of computed results for modified passive and active gears for a landing impact onto a smooth runway surface. $\theta = 10.5^{\circ}$; $\dot{z}_{c,g} = 2.7$ m/sec (8.8 ft/sec); $\dot{x}_{c,g} = 45.7$ m/sec (150 ft/sec).

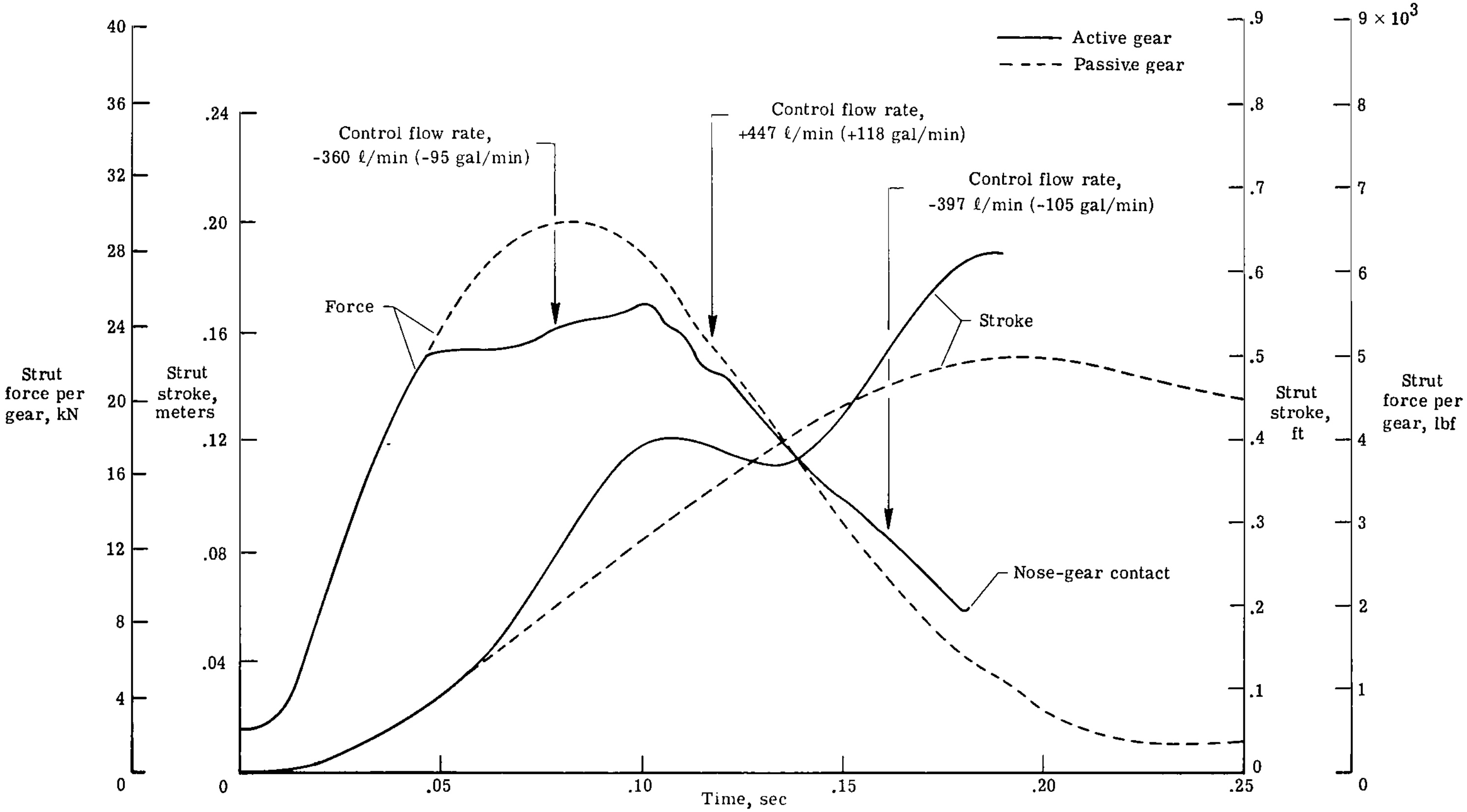

(b) Time histories of shock-strut force and stroke.

Figure 11.- Continued.

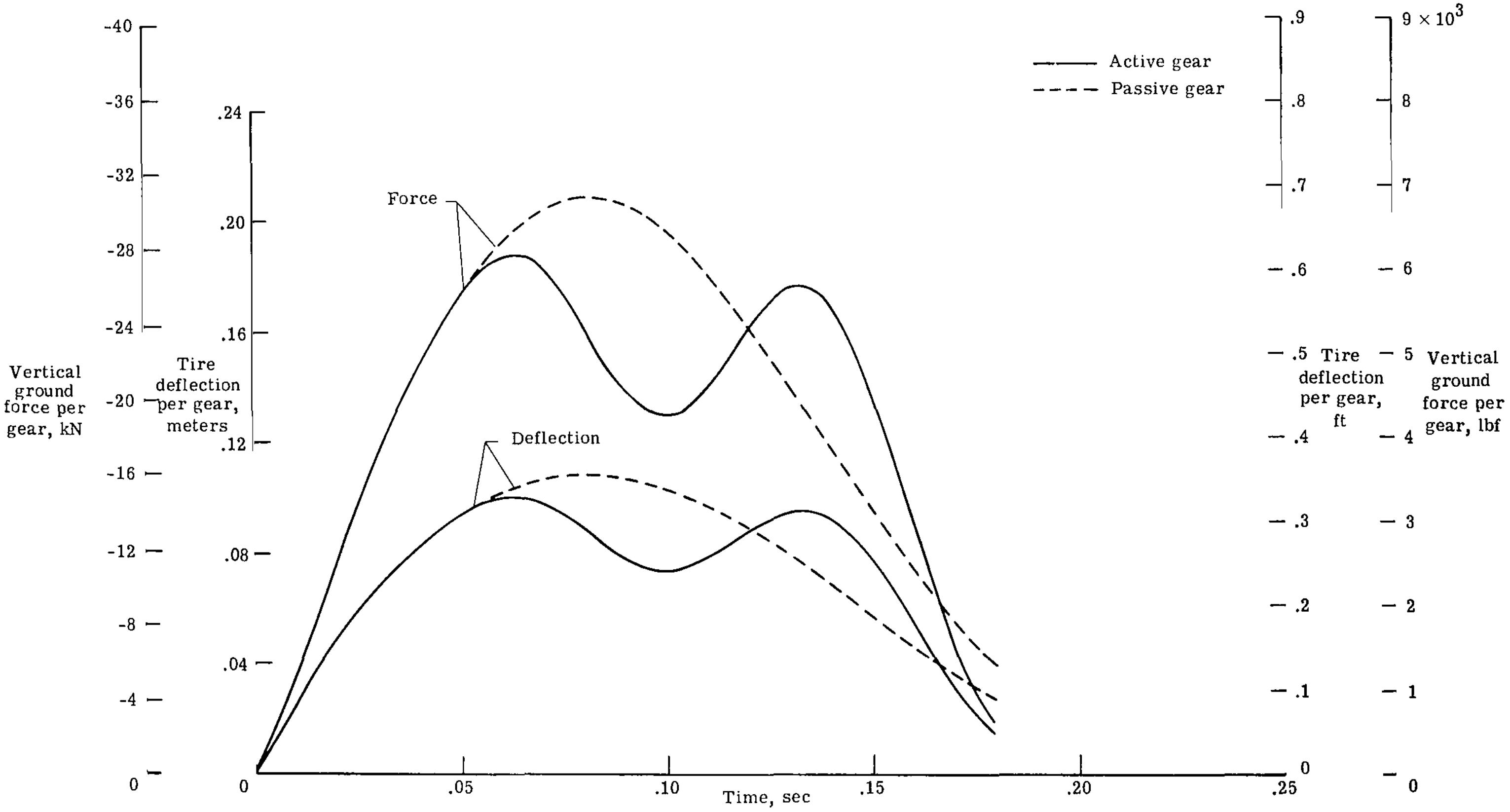

(c) Time histories of vertical ground force and tire deflection.

Figure 11.- Continued.

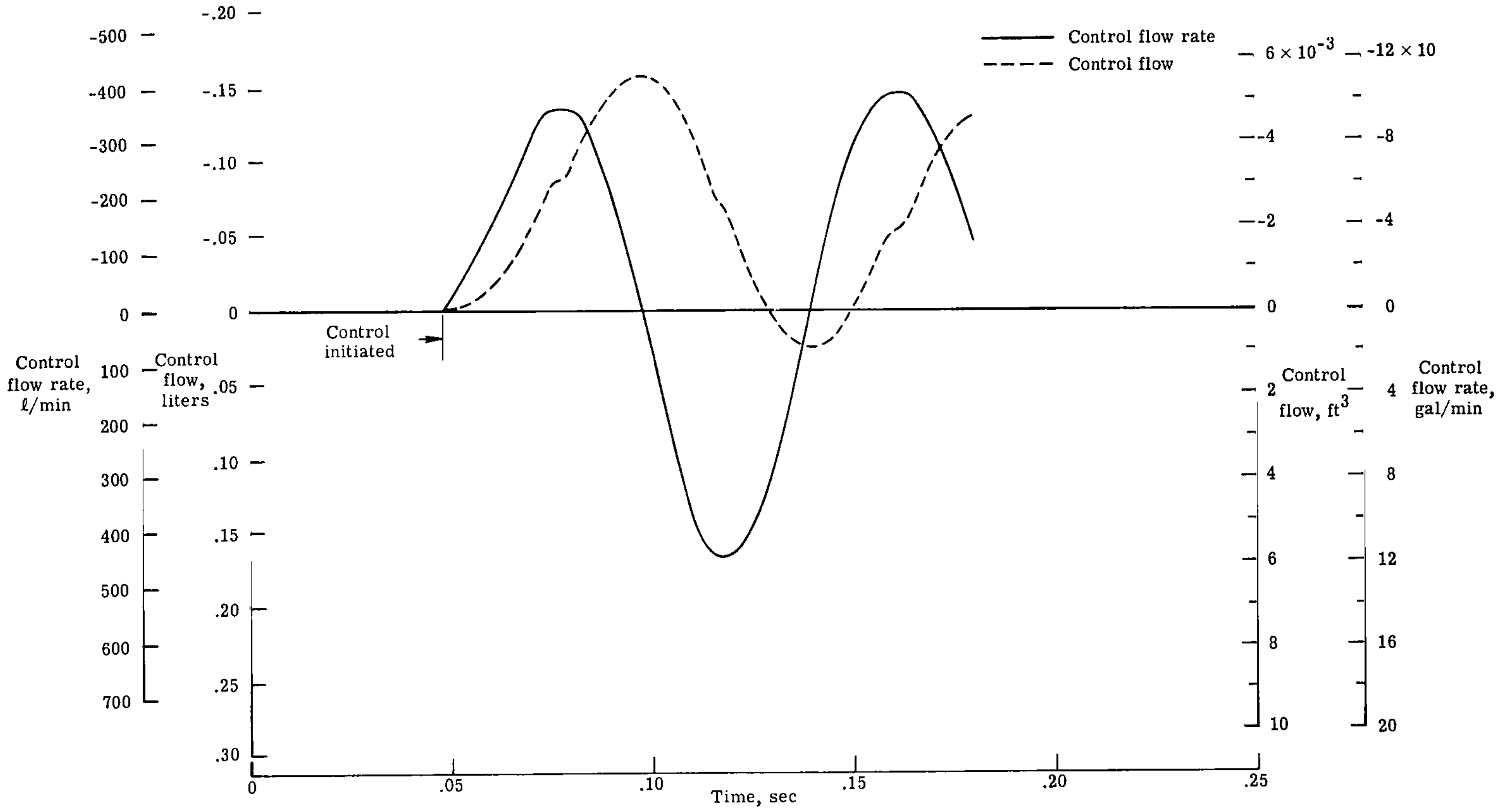

Figure 12.- Time histories of control flow rate and control flow for landing impact of active gear onto a smooth runway surface. $\theta = 10.5^{\circ}$; $\dot{z}_{c,g} = 2.7$ m/sec (8.8 ft/sec); $\dot{x}_{c,g} = 45.7$ m/sec (150 ft/sec).

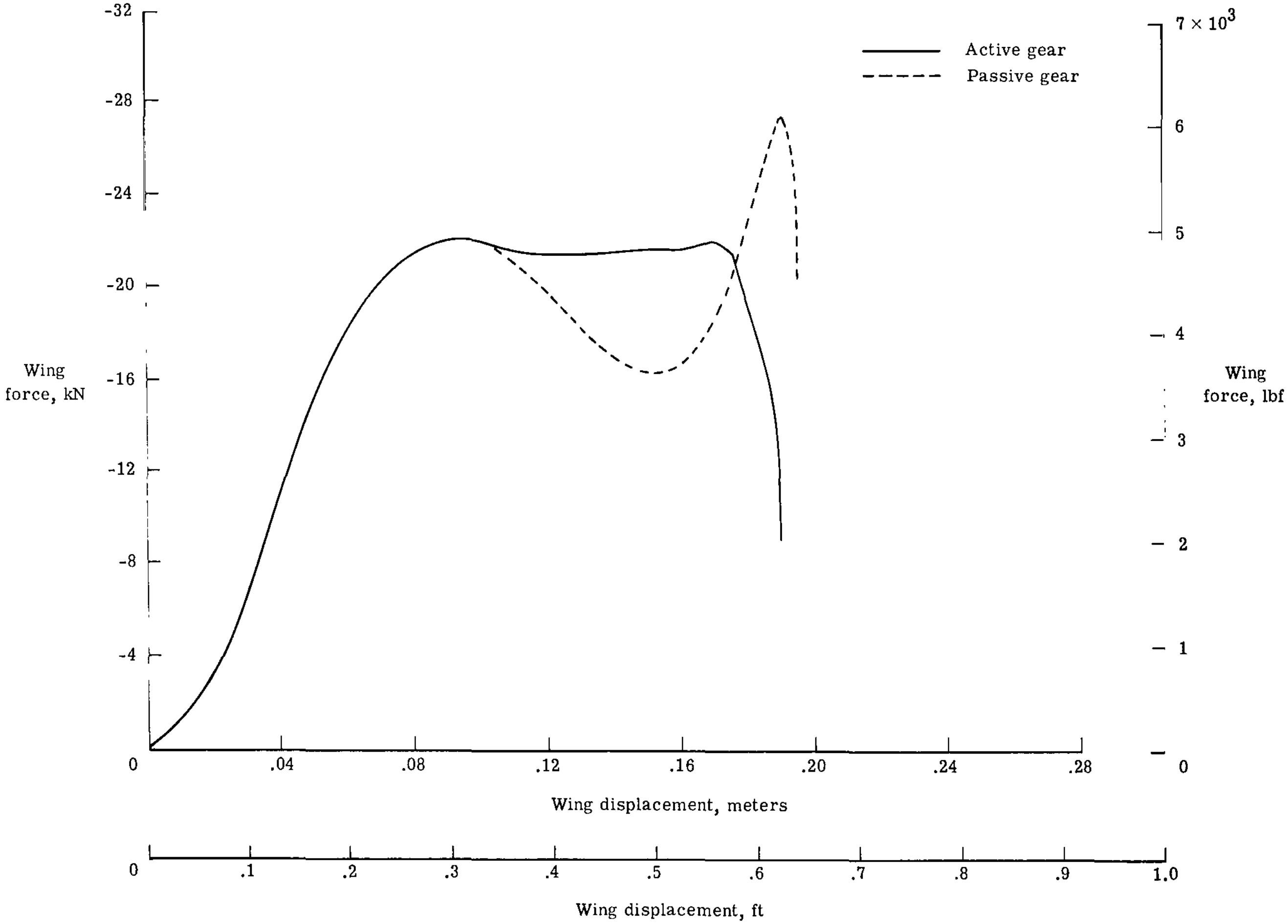

(a) Wing force as a function of wing displacement.

Figure 13.- Comparison of computed results for modified passive and active gears for a landing impact onto a sinusoidal runway surface. $\theta = 10.5^{\circ}$; $\dot{z}_{c,g} = 2.7$ m/sec (8.8 ft/sec); $\dot{x}_{c,g} = 45.7$ m/sec (150 ft/sec).

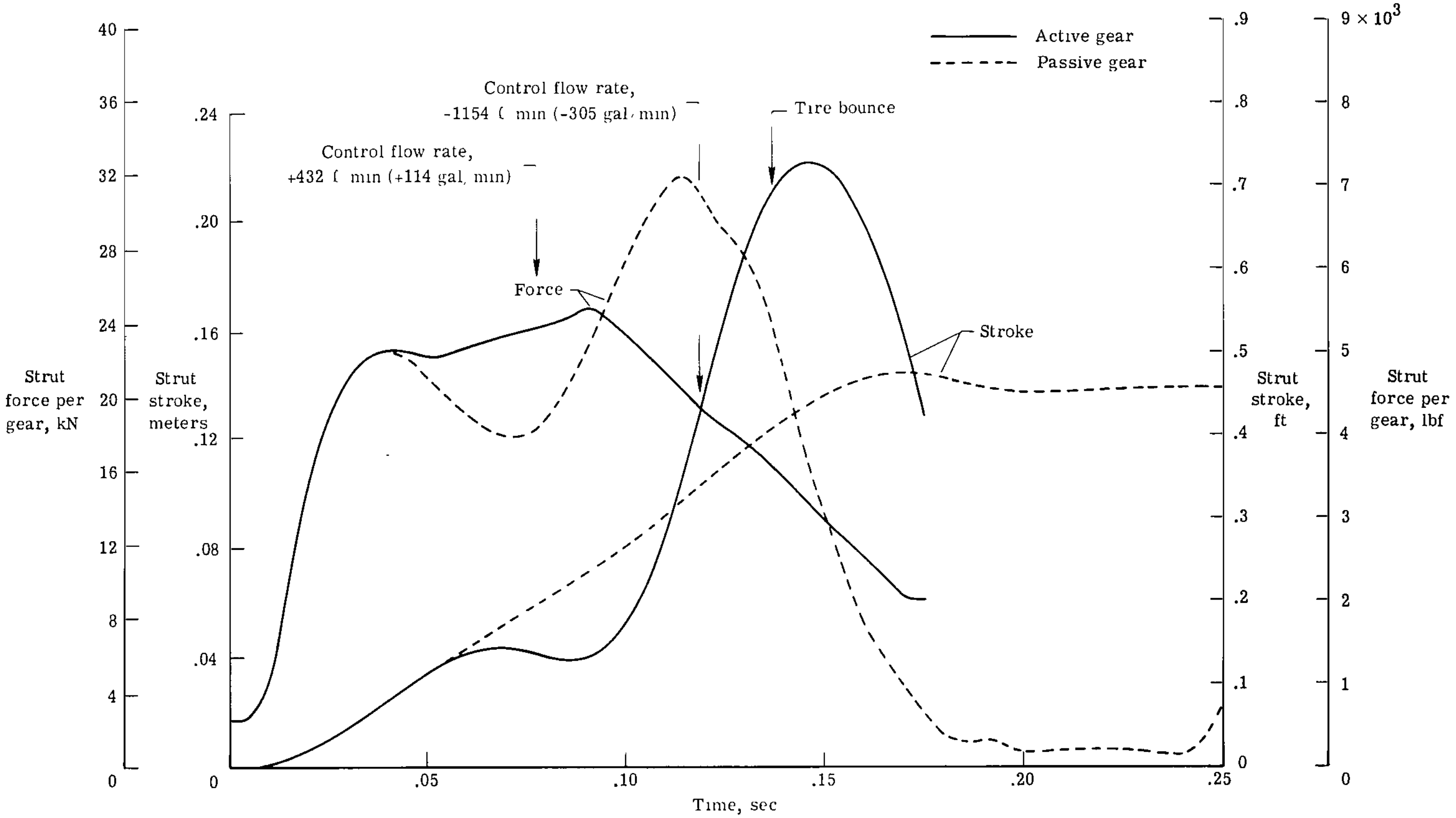

(b) Time histories of shock-strut force and stroke.

Figure 13.- Continued.

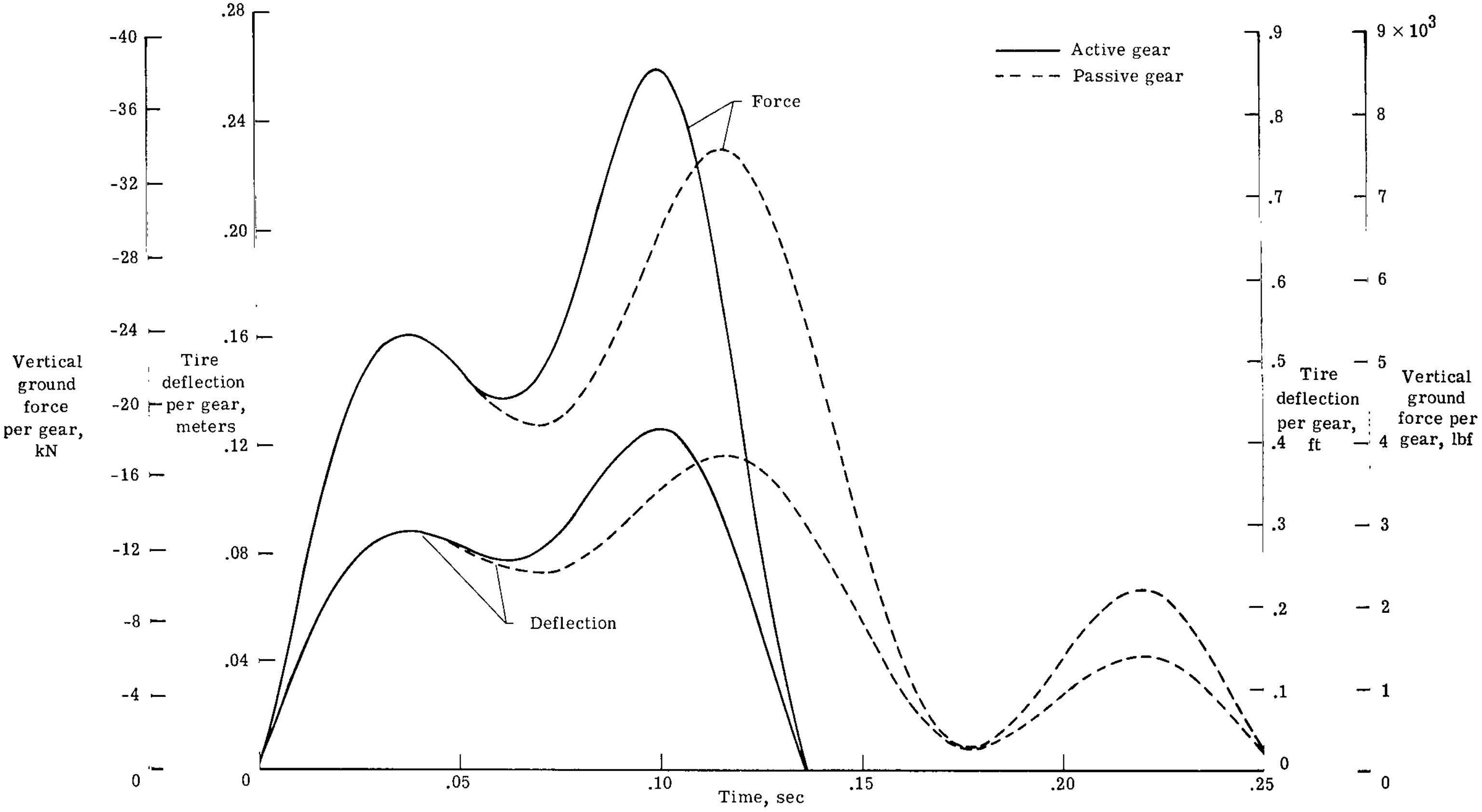

(c) Time histories of vertical ground force and tire deflection.

Figure 13.- Concluded.

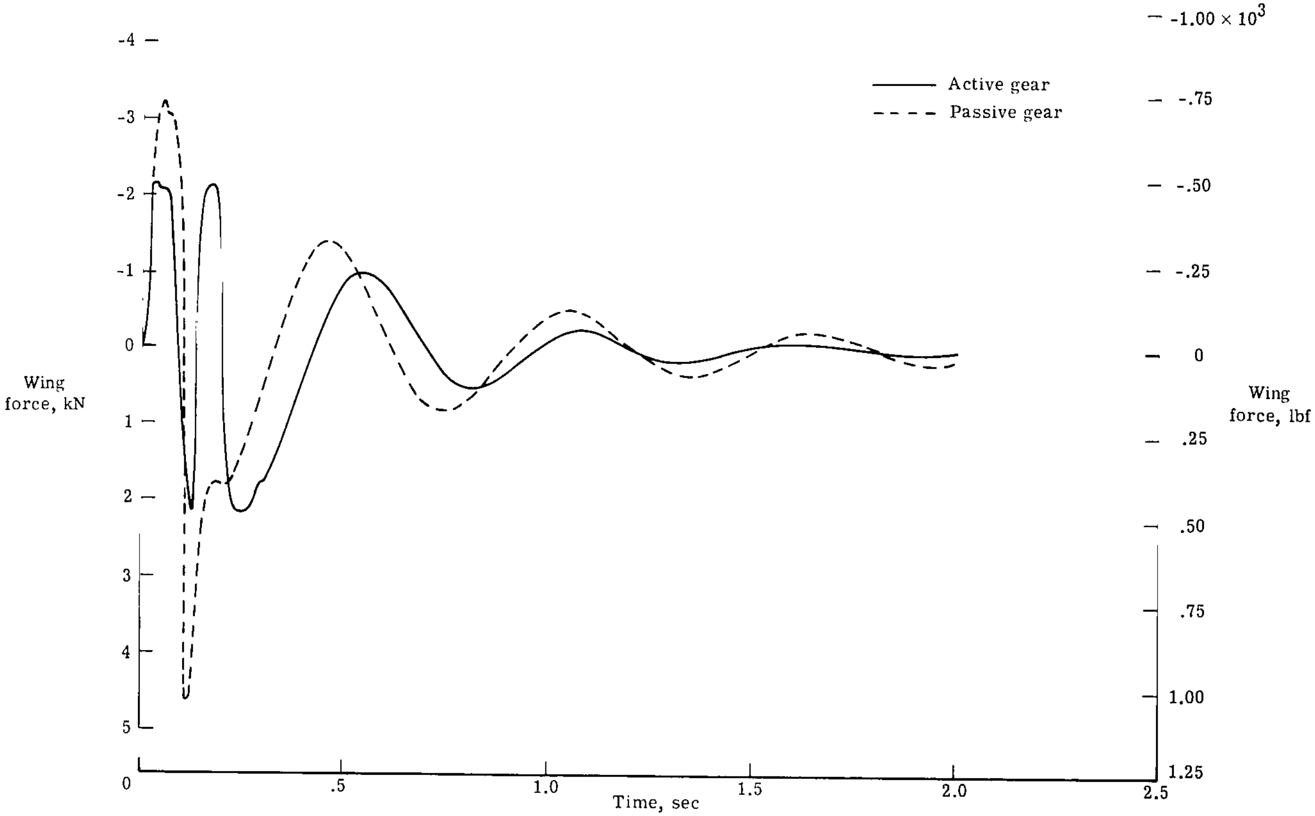

(a) Time histories of wing force.

Figure 14.- Comparison of computed results for active and passive gears for a landing roll-out after traversing a vertically discontinuous bump. $\theta = 0^{\circ}$; $\dot{z}_{c,g} = 0$ m/sec (0 ft/sec); $\dot{x}_{c,g} = 44.5$ m/sec (146 ft/sec).

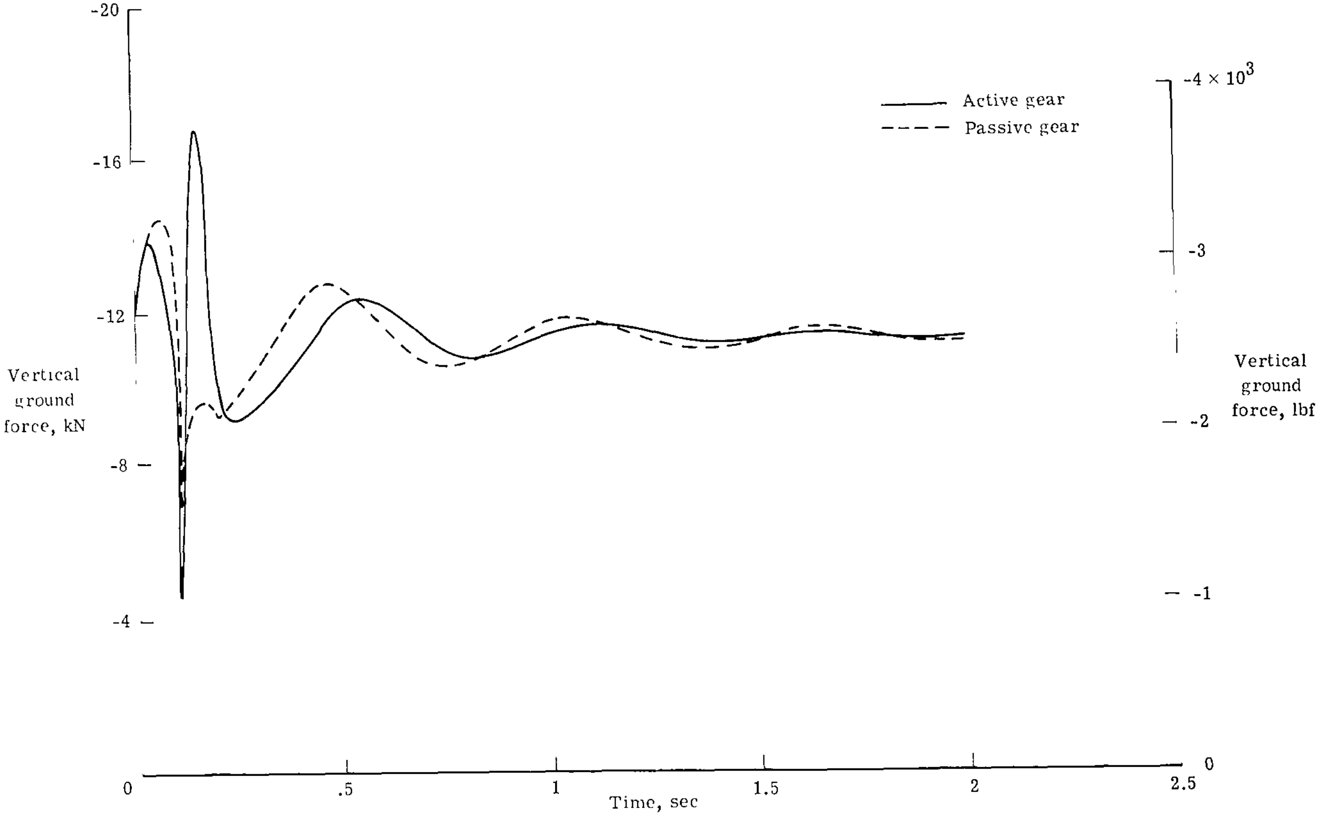

(b) Time histories of vertical ground force.

Figure 14.- Concluded.

NASA-Langley, 1976

L-10440

238 001 C1 U A 760123 S00903DS
DEPT OF THE AIR FORCE
AF WEAPONS LABORATORY
ATTN: TECHNICAL LIBRARY (SUL)
KIRTLAND AFB NM 87117

> *"The aeronautical and space activities of the United States shall be conducted so as to contribute . . . to the expansion of human knowledge of phenomena in the atmosphere and space. The Administration shall provide for the widest practicable and appropriate dissemination of information concerning its activities and the results thereof."*
>
> —NATIONAL AERONAUTICS AND SPACE ACT OF 1958

NASA SCIENTIFIC AND TECHNICAL PUBLICATIONS

TECHNICAL REPORTS: Scientific and technical information considered important, complete, and a lasting contribution to existing knowledge.

TECHNICAL NOTES: Information less broad in scope but nevertheless of importance as a contribution to existing knowledge.

TECHNICAL MEMORANDUMS: Information receiving limited distribution because of preliminary data, security classification, or other reasons. Also includes conference proceedings with either limited or unlimited distribution.

CONTRACTOR REPORTS: Scientific and technical information generated under a NASA contract or grant and considered an important contribution to existing knowledge.

TECHNICAL TRANSLATIONS: Information published in a foreign language considered to merit NASA distribution in English.

SPECIAL PUBLICATIONS: Information derived from or of value to NASA activities. Publications include final reports of major projects, monographs, data compilations, handbooks, sourcebooks, and special bibliographies.

TECHNOLOGY UTILIZATION PUBLICATIONS: Information on technology used by NASA that may be of particular interest in commercial and other non-aerospace applications. Publications include Tech Briefs, Technology Utilization Reports and Technology Surveys.

Details on the availability of these publications may be obtained from:

SCIENTIFIC AND TECHNICAL INFORMATION OFFICE
NATIONAL AERONAUTICS AND SPACE ADMINISTRATION
Washington, D.C. 20546